Biomaterials Science

ROYAL SOCIETY OF CHEMISTRY

PAPER

View Article Online
View Journal | View Issue

Check for updates

Cite this: *Biomater. Sci.*, 2026, **14**, 1441

3D printed hydrogel scaffolds for meniscal implant application: photo-crosslinkable urethane-based poly(ethylene glycol) as a case study

Ozge Begum Akalin,[a] Andrada Serafim,[b] Izabela-Cristina Stancu,[b] Catherine Van Der Straeten[c,d] and Peter Dubruel *[a]

The meniscus is one of the most injured structures in the human knee. Current clinical approaches do not adequately replace or regenerate the meniscus. Complete or partial meniscus removal leads to degenerative articular changes due to abnormal mechanical forces. Tissue engineering (TE) of the meniscus or developing non-tissue-engineered implants may offer efficient solutions. Yet, these approaches are challenging due to the requirement of a complex, non-toxic three-dimensional (3D) structure exhibiting adequate biomechanical and biological properties. In this study, we developed a porous 3D printed acrylate end-capped urethane-based poly(ethylene glycol) (AUP) hydrogel scaffold *via* extrusion-based 3D printing for meniscus implant application. With the aim to meet the required biomechanical properties, we studied the effects of two different scaffold variables. Indeed, in addition to the poly(ethylene glycol) (PEG) backbone molar mass (4000 *versus* 8000 g mol^{-1}), we also varied the scaffold design. The latter included variations in the scaffold pore size (200 μm, 350 μm and 500 μm) and the strut diameter (230 μm *versus* 370 μm). The morphology of the developed AUP hydrogel scaffolds was characterized *via* optical microscopy and nano-computed tomography (nano-CT), showing regular, porous, interconnected 3D hydrogel scaffolds. The physical properties of the scaffolds, including the gel fraction (75–89%), the swelling degree (230–500%) and the compressive modulus (0.5–3.2 MPa), depended on the scaffold design and the backbone molar mass. Surface analyses through X-ray photoelectron spectroscopy (XPS) showed the successful application of a photo-crosslinkable gelatin derivative (known as gel-MOD or gel-MA) on the printed AUP hydrogel scaffolds (as reflected by an N/C value of 0.06 for gel-MOD modified AUP *versus* no signal for non-modified AUP scaffolds). Live/dead staining and the MTT assay using human dermal fibroblasts (HDF) revealed the non-toxic behavior of the developed AUP scaffolds (90% cell viability). This study clearly demonstrates the potential of the developed AUP hydrogel scaffolds as meniscal implants, as the applied polymer and 3D printing technologies enable the development of non-toxic 3D porous scaffolds, of which both the cell-interactive character and the mechanical properties can be controlled.

Received 30th December 2024,
Accepted 14th December 2025

DOI: 10.1039/d4bm01730g

rsc.li/biomaterials-science

Open Access Article. Published on 21 January 2026. Downloaded on 5/27/2026 2:20:44 AM.
This article is licensed under a Creative Commons Attribution-NonCommercial 3.0 Unported Licence.

1. Introduction

The meniscus is situated in the knee and consists of the fibrocartilage tissue. It is comprised of two semilunar discs, the lateral and medial meniscus, positioned between the femoral surface and the tibial plateau.[1] Both components are connected to the tibial plateau, thus acting as a cushion between the femur and the tibia.[2] The blood flow in the meniscus goes from the periphery towards the center, which provides a gradient characteristic and structural anisotropy to the meniscus that divides the tissue into different zones. The peripheral vascular region is known as the red zone, showing a thick, convex morphology, whereas the innermost region is known as the white zone, exhibiting narrowing to a thin free edge.[3,4]

To date, the preferred treatment of meniscus tears involves surgery. Meniscal repairs can involve a partial meniscectomy, stitching of the torn pieces or meniscus transplantation. While arthroscopic meniscectomy is performed approximately 450 000 times annually in the US,[5] the recovery and/or the

[a]*Polymer Chemistry & Biomaterials Research Group, Center of Macromolecular Chemistry (CMAC), Ghent University, Krijgslaan 291, Building S4-bis, B-9000 Ghent, Belgium. E-mail: Peter.Dubruel@ugent.be*
[b]*Advanced Polymer Materials Group, University Politehnica of Bucharest, Bucharest, Romania*
[c]*International Society of Technology in Arthroplasty, 1246 P Street, Sacramento, CA 95814, USA*
[d]*HIRUZ – University Hospital Ghent, C. Heymanslaan 10, 9000 Ghent, Belgium*

Open Access Article. Published on 21 January 2026. Downloaded on 5/27/2026 2:20:44 AM. This article is licensed under a Creative Commons Attribution-NonCommercial 3.0 Unported Licence.

enhanced quality of life of the patients are low.[6–8] Furthermore, this treatment is not feasible if the tear is in the inner third of the meniscus, an area with limited vascularization and healing potential.[9] In addition, partial meniscectomy can lead to osteoarthritic degradation and eventually, to a need for a total knee joint replacement.[10,11] A meniscal scaffold that possesses the mechanical properties of the native tissue while exhibiting biocompatibility could delay or even prevent osteoarthritis, thus serving as a superior candidate for treatment. The biomechanical properties of the meniscus are directly correlated with the endurance to the forces exerted on the tissue and vary depending on the specimen location. The tensile modulus of the meniscus varies between the circumferential (100–300 MPa) and radial directions (10–30 MPa). On the other hand, the compressive modulus ranges between 0.7 MPa and 5 MPa depending on the specimen location, strain levels and testing methods.[4,12–16]

Scaffolds constituting materials of different types, natural, synthetic or a combination thereof, have already been investigated for meniscal tissue engineering (TE) or as meniscal implants.[6] While most natural scaffolds have an intrinsic biocompatibility, one of the drawbacks is their lack of adequate biomechanical properties, including rapid biodegradation, resulting in a mismatch with the time to be completely replaced by the newly formed tissue.[17] Moreover, batch-to-batch variation of natural polymers such as collagen, hyaluronic acid, alginate, agarose, gelatin, and silk is another drawback that can occur.[7] On the other hand, synthetic scaffolds can be manufactured custom-made in any shape, and they are typically batch-independent. They also have several advantages, including an almost limitless supply, as well as the potential to achieve the appropriate scaffold design, mechanical properties and scaffold geometry. However, crucial disadvantages of most of these scaffolds include minimal intrinsic biomechanical and bioactive properties since they lack the cell-adhesion domains present in many natural polymers.[18,19]

Since the meniscus is exposed to heterogeneous loading *in vivo* every day, appropriate mechanical properties are needed for a meniscus construct. However, synthetic polymers, such as polylactic acid (PLA) and polyglycolic acid (PGA), do not entirely mimic the mechanical properties of the natural meniscus, particularly due to premature partial degradation.[20,21] Indeed, they both exhibit a degradation time that is too fast, from one to two years, depending on the size and shape of the implant and the implantation site,[22] causing a significant decrease in mechanical properties. Poly-ε-caprolactone (PCL) shows a slower, more preferred degradation time of two to three years.[23] Polyurethanes (PU) are typically biocompatible but not cell interactive, and they do not prevent articular cartilage degradation after implantation.[18,24] To realize a successful substitute, polymeric scaffolds should exhibit optimal porosity, pore size, strut diameter, and mechanical properties (intimately linked to the scaffold design). Interconnectivity of the pores is an important property that the scaffold must possess to permit tissue ingrowth, diffusion of nutrients and removal of metabolic waste.[18,20,25,26] In addition, the polymer should be non-toxic to cells. In the case of fibrocartilage regeneration to create engineered meniscus tissue, the optimal scaffold pore size should range between 150 and 500 μm.[25,27,28]

Commercially available implants applied in the clinic include CMI (collagen meniscus implant), Actifit®, NUsurface® and Trammpolin®.[29] CMI, formerly known as Menaflex™, is composed of a collagen-glycosaminoglycan (GAG) matrix. Actifit® is an aliphatic PU based on PCL, while NUsurface® and Trammpolin® are polycarbonate-urethane (PCU) implants. CMI and Actifit® scaffolds are partial meniscal substitutes, whereas NUsurface® and Trammpolin® are total meniscal substitutes. Although CMI and Actifit® are biodegradable, NUsurface® and Trammpolin® are not. CMI requires cautious handling, and exhibits shrinkage over time and no histological remnants 5 to 6 years after implantation.[20,26] Long-term evidence on chondroprotection is needed for both CMI and Actifit® since failure was noticed in the chondroprotective ability of the implant.[26,30,31] NUsurface® and Trammpolin® aim to mimic the biomechanical function of the natural meniscus. However, clinical results in the short-term are discouraging, and further research in the long-term is required.[31–33] The first clinical trial of Trammpolin® was not promising, and modifications to the prosthesis design and fixation technique are needed.[34] Although these scaffolds are designed to mimic the function of the natural meniscus or stimulate the growth of new tissues, they need to be improved in terms of material and structure design.

It is thus clear that both natural materials and synthetic polymers show a distinct set of advantages and disadvantages. A possible solution can be obtained by combining them to link the high cell affinity and biocompatibility of various natural polymers with the superior mechanical strength and practicability of synthetic polymers. A tissue-engineered, patient-specific 3D printed meniscus with optimized mechanical and morphological properties, along with biocompatibility, can be a critical solution for meniscal injuries.

In this study, acrylate-terminated, urethane-based poly (ethylene glycol) (PEG) polymers (AUPs) are applied to investigate the 3D printing of AUPs towards meniscus TE.[35] PEG-based AUPs are photo-crosslinkable, semi-crystalline hydrogel precursors combining tunable mechanical properties with biocompatibility.[35] They are highly soluble in water (up to 9 mg ml^{-1}) and can absorb large amounts of water after crosslinking.[36] The physical properties of the crosslinked network can be tuned by varying the molar mass of the polymeric backbone. In addition, the AUP is UV reactive in the solid state, which provides unprecedented processing possibilities for 3D printing from the melt.[35] Moreover, urethane moieties enhance the hydrogel flexibility.[37]

The present work investigates the application of photopolymerized AUPs as porous scaffolds using melt printing, a pneumatic- and screw-driven micro-extrusion[38] for meniscal TE. This approach enables the fabrication of patient-specific scaffolds with tunable physical properties using the

 This journal is © The Royal Society of Chemistry 2026

Open Access Article. Published on 21 January 2026. Downloaded on 5/27/2026 2:20:44 AM. This article is licensed under a Creative Commons Attribution-NonCommercial 3.0 Unported Licence.

BioScaffolder device. Applying the photo-crosslinkable AUPs, the combination of parameters (temperature, pressure, speed, needle diameter) enabling printing will be determined. The developed scaffolds will be subjected to in-depth characterization, including gel fraction and swelling studies, scaffold visualization and determination of the mechanical properties, with the final aim of establishing structure–property relations. The final part of the work will comprise scaffold surface decoration using a cell-interactive gelatin layer while studying the initial biocompatibility of the (gelatin-modified) scaffolds.

2. Materials and methods

2.1 Materials

Butylated hydroxytoluene (BHT) was obtained from Innochem GMBH (Wardenburg, Germany). Bismuth neodecanoate (Valikat BI 2010) was purchased from Umicore (Brugge, Belgium), Bisomer PEA6 from GEO Specialty Chemicals (Southampton, UK), and gelatin type B from Rousselot (Ghent, Belgium). Dialysis membranes Spectra/Por 4 (MWCO 12–14 kDa) were obtained from Polylab (Antwerp, Belgium), while methacrylic anhydride, sodium hydroxide (NaOH) and potassium chloride (KCl) were obtained from Sigma-Aldrich (Diegem, Belgium). Poly(ethylene glycol) (PEG) 1000, 2000, 4000, 6000 and 8000 g mol^{-1}, PEG-diacrylate 6000 g mol^{-1}, isophorone diisocyanate (IPDI), phenothiazine (PTZ), triphenyl phosphite (TPP) and phosphoric acid were obtained from Sigma-Aldrich (Overijse, Belgium). 1-[4-2-Hydroxyethoxyphenyl]-2-hydroxy-2-methyl-1-propane-1-one (Irgacure 2959, I2959) was obtained from BASF (Antwerp, Belgium). Potassium phosphate monobasic (KH_2PO_4), sodium phosphate dibasic (Na_2HPO_4) and calcium chloride ($CaCl_2$, 96%) were provided by Acros (Geel, Belgium). Human dermal fibroblasts (HDF), Dulbecco's modified Eagle's medium (DMEM), fetal bovine serum (FBS) and L-glutamine were obtained from Sigma-Aldrich (Overijse, Belgium). Phosphate-buffered saline solution (PBS, pH 7.4, 0.1 M) and Dulbecco's phosphate buffered saline (DPBS) were purchased from Thermo Fisher Scientific (Geel, Belgium), while calcein-AM was obtained from AnaSpec (Liège, Belgium). Finally, propidium iodide, dimethyl sulfoxide (DMSO) and 3-(4,5-dimethylthiazol-2-yl)-2,5-diphenyl tetrazolium bromide (MTT) were obtained from Sigma-Aldrich (Overijse, Belgium).

2.2. Synthesis of acrylate-terminated, urethane-based poly (ethylene glycol) polymers (AUPs)

AUPs with five different molar masses were synthesized by reacting PEG (1000, 2000, 4000, 6000 and 8000 g mol^{-1}) with isophorone diisocyanate (IPDI) and monoacrylated oligo(ethylene glycol) in a 1 : 2 : 2 stoichiometric ratio. The synthesis is a two-step process.[35]

Prior to the synthesis, PEG was dried under vacuum. Next, the polymer was melted at 90 °C, and 500 ppm of butylated hydroxytoluene (BHT) with respect to the total polymer mass was added as a radical scavenger. In the first step, PEG was reacted with IPDI in a 1 : 2 stoichiometric ratio. As the reaction between IPDI and PEG is exothermal, the temperature was decreased to 65 °C prior to catalyst addition. Bismuth neodecanoate, 300 ppm with respect to the AUP amount, was added as a catalyst for the reaction occurring between the hydroxyl groups of PEG and the isocyanates. After the addition of the catalyst, the reaction temperature was kept at 75 °C. This reaction was performed under an inert atmosphere (N_2) until half of the isocyanates were consumed, as determined by measuring the NCO value *via* potentiometric titration. In the second step, the PEG-IPDI intermediate product was reacted with monoacrylated PEG in a 1 : 2 stoichiometric ratio under dry air in the presence of 300 ppm bismuth neodecanoate. After adding the catalyst, the temperature was raised to 80 °C. The reaction was considered complete when the NCO value was below the theoretical value of 0.02 meq g^{-1} reaction mixture, where the remaining half of the isocyanates have reacted in the second step. Phenothiazine (PTZ) and triphenyl phosphite (TPP), both in 500 ppm with respect to the AUP amount, were added as stabilizers when the reaction was completed. The product was collected and stored in an opaque bottle at room temperature.

2.3. Structural and physicochemical characterization of AUPs

2.3.1. Determination of the chemical structure *via* Fourier transform infrared (FTIR) spectroscopy. The chemical structures of the synthesized AUPs were analyzed by FTIR spectroscopy using a PerkinElmer Frontier FTIR mid-IR combined with an MKII Golden Gate setup equipped with a diamond crystal from Specac. The device was operated in attenuated total reflection (ATR) mode. The spectra of PEG, the intermediate product of the first reaction step (PEG-IPDI), and the final products (AUPs) were recorded with eight scans in the range of 800–4000 cm^{-1}.

2.3.2. Determination of the acrylate content *via* proton nuclear magnetic resonance (^{1}H-NMR) spectroscopy. The acrylate content of the AUPs was quantified *via* ^{1}H-NMR spectroscopy (Bruker Avance II Ultrashield) at 400 MHz using deuterated chloroform as the solvent. The spectra were analyzed using MestReNova software. Dimethyl terephthalate (DMT) was used as an internal standard to determine the acrylate content by comparing the integrations of the signal characteristic for the protons from the aromatic ring in DMT (δ 8 ppm) with the integration of the peaks corresponding to the acrylate protons (δ 5.85, 6.15 and 6.4 ppm).

2.3.3. Determination of the molar mass *via* gel permeation chromatography (GPC). The molar masses (MMs) of the AUPs were determined by GPC measurements on a Waters Alliance 2695 separation module with a Waters 2414 refractive index detector and equipped with PLGel Mixed-E polystyrene divinylbenzene GPC columns (particle size 3 μm). The MMs of the AUPs were determined as the number average molar mass (M_n) and the weight average molar mass (M_w) using a five-point calibration curve based on PEG standards (M_w range of 194–71 800 g mol^{-1}). The samples were prepared in high performance liquid chromatography (HPLC) grade chloroform

Open Access Article. Published on 21 January 2026. Downloaded on 5/27/2026 2:20:44 AM. This article is licensed under a Creative Commons Attribution-NonCommercial 3.0 Unported Licence.

(10 mg ml^{-1} AUP) and filtered (0.45 mm pore size) prior to analysis. The obtained results were analyzed using Waters Empower 2 software.

2.3.4. Determination of the thermal properties *via* thermogravimetric analysis (TGA) and differential scanning calorimetry (DSC). The thermal properties of the AUPs were determined by thermogravimetric analysis (TGA) using a TA Instruments Q-50 Thermogravimetric Analyzer and differential scanning calorimetry (DSC) using a TA Instruments Q-2000 device. For TGA, AUP samples (10–20 mg) were placed on a platinum sample pan and automatically loaded into the furnace. All analyses were performed under a nitrogen atmosphere. After equilibrating the samples at 35 °C, the AUPs were heated to 750 °C at a heating rate of 10 °C min^{-1}. The results were analyzed using TA Instruments Universal Analysis 2000 software.

For DSC, the AUPs (5–10 mg) were placed in T_0 aluminum pans and subsequently sealed with an aluminum T_0 lid. As a reference, an empty T_0 aluminum pan with a lid was used. Next, the samples were introduced into the device furnace, equilibrated at 35 °C and ramped at 10 °C min^{-1} up to 90% of the temperature value that corresponded to 1% mass loss in the preceding TGA analyses. The samples were kept isothermal for 3 min and were subsequently cooled at 10 °C min^{-1} down to −80 °C followed by another isothermal period of 4 min. Finally, the samples were reheated to the previous maximum temperature at 10 °C min^{-1} and were kept isothermal for 3 min. Data analysis was performed using TA Instruments Universal Analysis 2000 software.

2.4. Rheological analysis

Rheological characterization of the solvent-free molten AUPs was performed by small-strain oscillatory rheology using an Anton Paar Physica MCR 301 rheometer equipped with a Peltier element for temperature control. A parallel plate setup was used with a top plate diameter of 25 mm and a gap setting of 0.3 mm. The viscosity of AUPs was monitored by applying the molten polymers between the two plates. First, strain sweeps were recorded to establish the linear viscoelastic range of the materials by increasing the strain from 0.01% to 100% while applying a frequency of 1 Hz. Next, the mechanical spectrum of the AUPs was obtained by increasing the frequency from 0.01 to 10 Hz under a constant strain of 0.1%. After the evaluation of the viscoelastic range characteristic for the molten polymers, a strain of 0.1% and an oscillation frequency of 1 Hz were selected. This was followed by recording the viscosity of the molten AUPs at a shear rate of 10% for 1 min within the temperature range of 40–100 °C.

2.5. Extrusion-based 3D printing of AUP scaffolds

AUP scaffolds were printed with the BioScaffolder (SysEng, Germany), a 3D dispensing technique that allows layer-by-layer deposition of a three-dimensional construct. The nozzle operates pneumatically, and its dispensing head moves in three dimensions while the collecting plate is stationary. The strut thickness can be altered by varying the material viscosity, the deposition speed (speed of the printing head), the nozzle diameter and/or the applied pressure. The scaffolds were designed with Tinkercad, while PrimCam (Sys-Eng, Germany) was used to create the final structure. Porous scaffolds with 10 × 10 × 5 mm^3 dimensions were printed from the AUP melt since the polymers are UV reactive in the solid state. Printing was performed from the melt in the presence of 2 or 4 mol% Irgacure 2959 photoinitiator (PI) relative to the acrylates present for AUPPEG4K (AUP, the 4000 g mol^{-1} PEG derivative) (0.33 mmol acrylate per g AUP) and AUPPEG8K (0.16 mmol acrylate per g AUP), respectively. For 3D printing, the evaluated temperature range was 40 °C–100 °C while the inner diameter of the printing needle was 200 μm (gauge 27) and 250 μm (gauge 25) for AUPPEG4K and AUPPEG8K, respectively. The selected overlay pattern was 0°–90°, combined with 3 different pore sizes (220, 370 and 520 μm) and 2 different strut diameters (230 and 370 μm). Different strut diameters were obtained by altering the deposition speed and the applied pressure, whereas different pore sizes were realized by changing the inter-strut distance. The speed of the printing head and applied pressure were 250 mm min^{-1} and 3 bar for 370 μm struts, while the speed and pressure were 500 mm min^{-1} and 5 bar for 230 μm struts. After 3D printing, the scaffolds were exposed to UVA-irradiation from the top and bottom (8 mW cm^{-2}) for 60 min. The samples were kept in double distilled water for 72 hours to reach equilibrium swelling and remove any unreacted AUP.

2.6. Physicochemical characterization of the AUP scaffolds

2.6.1. Determination of scaffold morphology. To evaluate the architecture of the scaffolds (pore and strut size determination), optical microscopy images were recorded using a Zeiss Axiotech microscope with ZEN software (Zeiss, Oberkochen, Germany). The data were quantified using ImageJ software. The pore sizes of at least 3 different scaffolds were measured, and at least 5 different pores and struts were analyzed for each scaffold. Pore sizes and strut diameters were measured from the top view images of the scaffolds.

To evaluate the porosity of scaffolds during compression, nano-CT analysis was performed using a SkyScan 2211 high-resolution X-Ray nanotomograph (Bruker Micro-CT, Belgium) equipped with a compression cell of 440 N. The sample was mounted on the lower plate, which was gradually raised at a speed of 6 μm s^{-1}. An initial scan was performed (S0) before any stress was applied on the sample and a subsequent scan was performed at 0.3 mm deformation (S1). All samples were scanned in nanofocus mode, using a Flat Panel with a camera binning of 1 × 1 and a pixel size of 10.5 μm. The source voltage and current were set to 50 kV and 360 μA, respectively. The images were registered with a rotation step of 0.2° and an average of 4 frames at an exposure time of 700 ms, resulting in a scanning time of approximately 1 hour for each sample. The resulting cross-sections were processed using CT NRecon software (version 1.7.1.6) and subsequently reconstructed using CTVox (version 3.3.0r1403). DataViewer software (version 1.5.4.6) was used to analyze the projections of the samples. The analysis of the scaffold's morphometric parameters was

 This journal is © The Royal Society of Chemistry 2026

Open Access Article. Published on 21 January 2026. Downloaded on 5/27/2026 2:20:44 AM.
This article is licensed under a Creative Commons Attribution-NonCommercial 3.0 Unported Licence.

performed using the software CTAn (version 1.18.4.0+). All scanning, reconstruction and visualization parameters were kept constant for the analyzed samples. In addition, the porosity of the 3D printed AUP scaffolds was calculated from the following theoretical approach[39,40] as shown in eqn (1) for the comparison of the porosity of AUP scaffolds to the nano-CT based findings.

$$\text{Porosity}\,(\%) = \begin{cases} P \geq 0, & P = \left(1 - \frac{\pi}{4}\frac{{d_1}^2}{d_2 d_3}\right) \times 100, \\ P < 0, & P = 0 \end{cases} \qquad (1)$$
$$d_1, d_2, d_3 > 0, \quad \frac{d_2}{d_1} \in [0, \infty], \quad \frac{d_3}{d_1} \in [0, 1]$$

where P is the scaffold porosity, d_1 is the strut diameter, d_2 is the inter-strut distance and d_3 is the layer thickness within each different structure.

2.6.2. Determination of the swelling degree and the gel fraction. First, the scaffolds were weighed to determine the dry mass, followed by immersion in Milli-Q water at room temperature for 72 hours to reach equilibrium swelling. During this incubation, the medium was refreshed every day. Prior to weighing the swollen scaffolds, excess water was dabbed off the surface. Next, the scaffolds were freeze-dried to obtain the dry mass. The dry mass, the hydrated mass and the mass after freeze-drying of the samples were recorded as W_d, W_s and W_{fd}, respectively. The swelling degree (SD) and the gel fraction (GF) of the scaffolds were calculated from eqn (2) and (3).

$$\text{SD}\,(\%) = \frac{W_s - W_{fd}}{W_{fd}} \times 100 \qquad (2)$$

$$\text{GF}\,(\%) = \frac{W_{fd}}{W_d} \times 100 \qquad (3)$$

2.6.3. Mechanical characterization of the scaffolds using compression tests. The mechanical properties of the 3D printed scaffolds were studied using a Tinius Olsen 5 ST device operated by the Horizon software. The scaffolds ($1 \times 1 \times 0.5$ cm^3) were swollen to equilibrium before the uniaxial unconfined compression testing. Samples were compressed at a rate of 10 mm min^{-1} until failure. A load cell of 500 N was applied and 0.5 N was selected as a preload prior to data collection. Stress (MPa) *versus* strain (%) plots were recorded, and the compressive stress at break and the deformation at break were obtained from the point at which the scaffold fails, while the compressive modulus was calculated from the slope of the linear part of the curve under physiological strains (10–12%).

2.6.4. Biofunctionalization of AUP scaffolds using photocrosslinkable gelatin (gel-MOD). Gelatin containing photocrosslinkable methacrylamide side groups (gel-MOD) was prepared according to a previously reported protocol.[41] The AUP scaffolds were subjected to an argon plasma treatment in a cylindrical dielectric discharge plasma reactor (Model Femto, version 3, Diener Electronic, Germany) for 30 s. The argon pressure was maintained at 0.8 mbar with the applied power of 100 W. The treated scaffolds were exposed to ambient atmosphere for 10 min to enable the reaction of free radicals on the surface with oxygen to form (hydro)peroxides, as reported previously.[42] The plasma-activated scaffolds were immersed in a 2 w/v % gel-MOD (degree of substitution, DS of 97%) solution in double distilled water, containing 2 mol% Irgacure 2959 (relative to the amount of methacrylamides starting from a stock solution containing 8 mg ml^{-1} Irgacure 2959) at 40 °C under continuous magnetic stirring. Next, they were subjected to a vacuum treatment for 3 hours to ensure complete intrusion of the gel-MOD solution throughout the pores of the scaffolds. Afterwards, the scaffolds were placed on glass slides and exposed to UV-A irradiation from both sides (8 mW cm^{-2}) for 60 min to induce covalent crosslinking followed by dissolution of any un-crosslinked gel-MOD in double distilled water at 40 °C for 60 min.

2.6.5. Surface atomic composition *via* X-ray photoelectron spectroscopy (XPS). XPS measurements were performed on an ESCA S-probe VG monochromatized spectrometer with an Al Ka X-ray source (1486 eV). A survey scan spectrum was collected and from the peak-area ratios, the relative elemental composition of the material top layer was determined. The N 1s core signal was used to indicate gel-MOD deposition onto the AUP scaffolds, as described before.[42] XPS-micromapping was also performed on the AUP scaffolds to analyze the distribution of nitrogen on the scaffold surface and cross-section. Each spot measured by XPS was selected at intervals of 120 μm and 480 μm vertically and horizontally, respectively, giving 15 measurement points in total. XPS data were analyzed using CasaXPS software and the gel-MOD distribution was plotted using MATLAB (R2023b, The MathWorks).

2.7. *In vitro* cytotoxicity testing using human dermal fibroblast (HDF) cells

HDF cells were cultured at 37 °C under 5% CO_2 in fibroblast complete growth medium (all-in-one ready-to-use medium) that contains serum. No extra serum or antibiotics were added to the medium. The cells were split after a cell confluence of 80–90% was reached. PCL scaffolds were used as a control material. PCL, AUP and gel-MOD coated AUP scaffolds were sterilized using ethylene oxide (cold cycle, KU Leuven Hospital, Leuven). The indirect cytotoxicity tests were performed according to ISO 10993-5 standards. To this end, the surface area to volume ratio used for the extraction medium was 3 cm^2 ml^{-1}, as specified by ISO norms.[43] Prior to cell seeding, the scaffolds were incubated in PBS at room temperature for 2 days to reach equilibrium swelling, followed by incubation in cell culture medium for 1 day. Cells were seeded at a density of 34 000 cells per well in a 24-well plate. After 24 hours, the culture medium was removed and replaced with 1 ml of extraction medium for each well. Cell viability was evaluated 48 hours later qualitatively and quantitatively by calcein-AM/propidium iodide staining and MTT assay, respectively.

2.7.1. Calcein-AM/propidium iodide staining. Calcein-AM/propidium iodide staining was performed to visualize the live and dead cells. For this purpose, the extraction medium was removed, after which 0.5 ml of suspension medium containing 1 ml of PBS, 2 μl calcein-AM (1 mg ml^{-1}) and 2 μl propidium

Open Access Article. Published on 21 January 2026. Downloaded on 5/27/2026 2:20:44 AM. This article is licensed under a Creative Commons Attribution-NonCommercial 3.0 Unported Licence.

iodide (1 mg ml^{-1}) was subsequently added. After 10 minutes of incubation protected from light, the viability of the cells was visualized *via* a fluorescence microscope (Thermo Fisher EVOS XL Core and EVOS M7000) with a green fluorescent protein (GFP) filter for calcein-AM to visualize the living cells and a Texas red (TxRed) filter for propidium iodide to visualize the dead cells. Cells cultured on tissue culture plastic were taken as a positive control.

2.7.2. MTT assay for cell viability. The colorimetric MTT assay was performed to quantify cell viability using 3-(4,5-dimethylthiazol-2-yl)-2,5-diphenyl tetrazolium bromide (MTT). To this end, the extraction medium was replaced with 0.5 ml (0.5 mg ml^{-1}) MTT reagent and the cells were incubated for 4 h at 37 °C. The MTT reagent was removed and replaced with 0.5 ml of lysis buffer (10 vol% Triton X-100 in sterile water, followed by 1 : 10 dilution in isopropanol/0.04 N HCl) and placed on an orbital shaker at 37 °C for 30 min. Finally, the absorbance of the resulting solution was measured at 580 nm *via* a microplate absorbance reader (PerkinElmer EnVision). Measurements were performed at the same time points as the microscopic evaluation and each experiment was conducted in triplicate.

2.8. Statistical analysis

Triplicate samples were used for the analyses. Statistical analysis was performed using the Analysis ToolPack for Excel, while statistically significant differences were determined *via* one-way ANOVA with Tukey's *post-hoc* test using Real-Statistics add-in for Excel. $p < 0.05$ was considered to indicate a significant difference between the constituents. The averages and standard deviations are reported in each figure.

3. Results and discussion

Considering the synthetic scaffolds, PCL-based[23,27,30,31,44,45] and polyurethane-based polymers[10,46–50] are among the most frequently investigated polymers as meniscal substitutes. As an alternative strategy, the use of hydrogel materials has been proposed due to their semi-liquid nature, which enables a great resemblance to living tissues.[51] To date, they have been rarely utilized for meniscus TE or as meniscal implants since their mechanical properties are generally inferior.[6] In addition, many synthetic hydrogels also lack cell-adhesive properties.

To meet this stringent need in the field, we aimed to apply acrylate end-capped urethane-based PEG polymers (AUPs) as a novel hydrogel. AUPs are semi-crystalline hydrogel precursors which combine successful crosslinking in the solid state, excellent biocompatibility and tunable mechanical properties (through variations in molar mass, polymer type, type and number of end group(s), *etc.*). The UV reactivity in the solid state opens unprecedented processing capabilities for melt-based manufacturing with subsequent solid state photopolymerization.[35] AUPs were previously investigated as TE scaffolds *via* indirect solid freeform fabrication[52] and bioplotting of AUP/LAPONITE® inks,[53] yet the processability of AUPs *via* direct printing from the melt remains largely unexplored. The application as a meniscal substitute is completely new.

3.1. Structural and physicochemical analysis of the AUP hydrogel precursors

The AUPs (chemical structure depicted in Fig. 1A) were synthesized by reacting PEG (1000, 2000, 4000, 6000 or 8000 g mol^{-1}, abbreviated as PEG1K to PEG8K) with 2 equivalents of IPDI followed by 2 equivalents of monoacrylated oligo(ethylene glycol). The reaction scheme of the AUP synthesis is given in Fig. S1. As an example, the FTIR spectra of the starting PEG4K, the intermediate product resulting from the first reaction step (PEG4K-IPDI), and the final AUP hydrogel precursor (AUPPEG4K) are shown in Fig. 1B. At the end of the first reaction step, the absorption bands corresponding to the N–H stretch (3330 cm^{-1}), the C═O stretch (1720 cm^{-1}), the amide II (1530 cm^{-1}) and the amide III bands (1300 cm^{-1}) can be identified in the spectrum of the PEG-IPDI, confirming the urethanization reaction. In addition, the characteristic absorption band (2260 cm^{-1}) of the isocyanate groups was observed in the PEG-IPDI intermediate product. This absorption band completely disappeared at the end of the second reaction step, confirming that all free isocyanates were consumed at the end of the reaction for AUPs. Moreover, the characteristic absorption bands corresponding to the acrylate functional groups, such as the C═C stretch of the acrylate groups (1635 cm^{-1}) and the C–O stretch of the acrylate esters (1200 cm^{-1}) are visible in the spectra. The FTIR spectra of the other AUPs, shown in Fig. S2, confirm the data obtained for the AUPPEG4K synthesis.

The ^{1}H-NMR spectrum of the AUPPEG4K hydrogel precursor is shown in Fig. 1C.[35] The signals between δ = 0.7 and δ = 2.0 ppm correspond to the methyl and the methylene protons in the cyclic part of IPDI, where the signals at δ = 3.3 and δ = 3.8 ppm are attributed to the methylene protons present in the PEG backbone and the spacers. The signal corresponding to the methylene protons of PEG that are adjacent to the hydroxyl functionalities shifted from δ = 3.61 to δ = 4.15 ppm (a to a′) as a result of the urethanization reaction, whereas the signal attributed to the methylene protons of spacers that are adjacent to the acrylate groups shifted from δ = 3.61 to δ = 4.26 ppm (a to a″). The signals at δ = 5.8, δ = 6.1 and δ = 6.3 ppm belong to the acrylate protons. The ^{1}H-NMR spectra of the other AUPs are shown in Fig. S3A and confirm successful syntheses for all AUP derivatives obtained.

The data from the ^{1}H-NMR spectra were used to determine the acrylate content for all AUPs. As an example, the ^{1}H-NMR spectrum of AUPPEG4K with an internal standard is shown in Fig. S3B. The acrylate content was calculated as the ratio of the signals from the acrylate protons to the benzene protons present in the standard compound dimethyl terephthalate (DMT). An exponential decrease in the acrylate content of AUPs was observed due to an increase in the backbone molar mass (Table 1 and Fig. S3C), as theoretically anticipated. Using the PEG backbone hydroxyl content (derived from Fig. S4), the

 This journal is © The Royal Society of Chemistry 2026

Open Access Article. Published on 21 January 2026. Downloaded on 5/27/2026 2:20:44 AM.
This article is licensed under a Creative Commons Attribution-NonCommercial 3.0 Unported Licence.

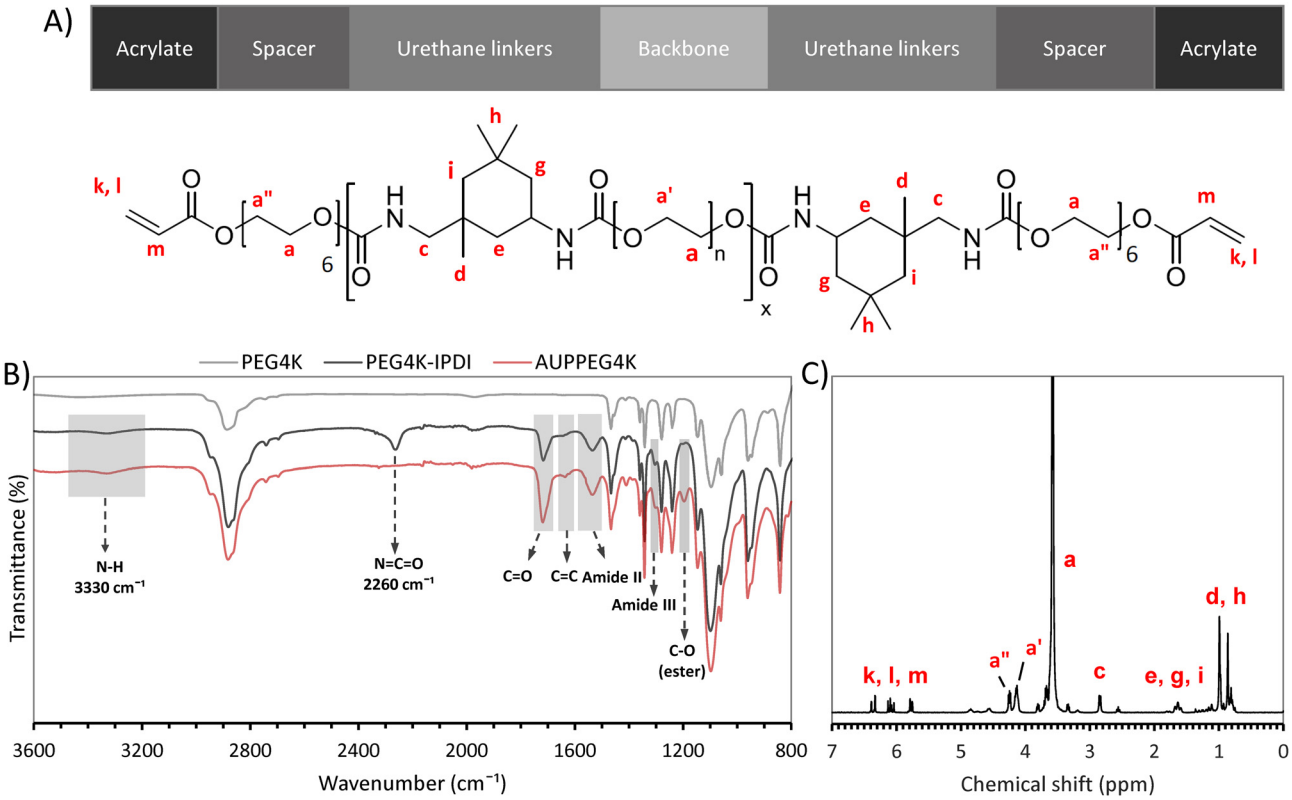

Fig. 1 Structure of the acrylate-terminated, urethane-based PEG polymer (AUP) (*n* depends on the molar mass of the backbone, *x* = 1–3). (A) Molecular structure of the AUP. (B) FTIR spectra of the starting PEG, the intermediate product (PEG-IPDI) and the final AUP. (C) ^{1}H-NMR spectrum of the AUP. In (B) and (C), the 4000 g mol^{-1} PEG derivative is shown (indicated as AUPPEG4K).

acrylate contents corresponded with degrees of substitution values between 92% and 97% (Table S1) for AUPs, indicating an almost complete end group modification.

In the next step, the molar mass and the thermal properties of the developed AUP macromonomers were assessed. The polymer properties are of paramount importance as the printing temperature window (for extrusion-based printing from the melt) depends on both properties (*cf.* thermal stability and viscosity of the polymer melt). The GPC data (values in Table 1, GPC traces in Fig. S5) indicate that the molar mass (M_n) of the AUPs increased with an increase in the PEG backbone molar mass, as expected. In addition, the molar mass of AUPs developed was almost twice that of the molar mass of the PEG used as one of the building blocks in the AUP synthesis. This can be explained by the repetition of the "PEG-IPDI" parts due to the low selectivity of the bismuth-based catalyst used during the AUP synthesis. This catalyst was selected due to its low toxicity.[54] A low selectivity of the catalyst results in the reaction of the primary as well as the secondary isocyanate groups of IPDI in the first reaction step, which leads to the formation of repeating "PEG-IPDI" units and hence a two-fold higher molar mass as compared to the PEG molar mass.

The degradation temperature of the AUPs was measured using TGA as the temperature at which 1% mass loss of the polymer occurred (Fig. S6). The crystallization temperature (T_c)

Table 1 Overview of the physicochemical characteristics of the developed AUPs

Material	AUPPEG1K	AUPPEG2K	AUPPEG4K	AUPPEG6K	AUPPEG8K
Acrylate content (mmol g^{-1} AUP)	0.81	0.55	0.34	0.24	0.17
Degree of substitution (%)	93	92	97	96	94
M_n (g mol^{-1})	2300	5600	9200	13 100	17 500
M_w (g mol^{-1})	4200	8000	13 600	19 800	27 000
Dispersity ($Đ$)	1.83	1.43	1.48	1.51	1.54
Degradation temperature[a] (°C)	145	168	210	222	256
T_c (°C)	[b]	10.0	29.2	33.5	36.8
T_m (°C)	[b]	34.4	49.3	52.6	54.6

[a] Degradation temperature at which 1% mass loss of the polymer occurred. [b] T_c and T_m could not be detected in AUPPEG1K.

Open Access Article. Published on 21 January 2026. Downloaded on 5/27/2026 2:20:44 AM. This article is licensed under a Creative Commons Attribution-NonCommercial 3.0 Unported Licence.

and the melting temperature (T_m) of the AUPs were measured using DSC. With an increasing molar mass (going from AUPPEG1K to AUPPEG8K), the degradation temperature, the T_c and the T_m increased (Table 1, derived from the DSC thermograms shown in Fig. S7).

This trend in thermal properties with an increase in molar mass is similar to previously reported PEG-diacrylate systems[55,56] and other polymers.[57,58] Indeed, the tendency of a polymer to crystallize decreases with increasing molar mass as longer chains are more hampered to align, forming crystalline domains. Higher molar mass polymers require a higher temperature for the melting and the degradation processes, given the larger number of chain entanglements/chain interactions compared to their lower molar mass counterparts.

Considering the melting temperatures of some AUPs being below body temperature, AUPPEG1K and 2K were excluded from further application in this study. To establish structure–property relations, all further tests were performed on the remaining AUPs with the highest and the lowest molar mass (AUPPEG4K and 8K).

3.2. Applicability of extrusion-based printing for AUP melts and parameter optimization

Following the structural and physicochemical evaluation (see section 3.1), the developed AUPs were applied in 3D printing experiments. To investigate the applicability of AUPs for extrusion-based 3D printing as a meniscal scaffold, we varied the AUP molar mass, the scaffold design (pore size and the strut diameter) and the processing conditions (printing temperature, pressure, speed and needle diameter). In addition, the effect of Irgacure 2959 as a photoinitiator in an AUP-type dependent concentration (see section 2.5) was evaluated. The selected scaffold design for the printing experiments is shown in Fig. 2. The design combines strut diameters of either 230 or 370 μm with pore sizes of 220, 350 or 520 μm.

3.2.1. Determination of the optimal temperature and pressure for 3D printing. AUP melts were characterized using a rotational rheometer in the temperature range between 40 and 100 °C to determine the optimal viscosity (Fig. S8). However, the upper limit of 80 °C was chosen to avoid premature thermal crosslinking during the 3D printing of AUP melts. In this temperature range, the higher temperatures resulted in a too low viscosity (approximately 11 Pa s for AUPPEG4K at 80 °C), leading to material outflow (strut deformation) and printed layers that could not cool down quickly enough for the next layer to be deposited, even at low printing speeds. The optimal viscosity for printing AUPPEG4K was between 20 and 30 Pa s. For AUPPEG4K, a temperature of 57 °C was selected as the final printing temperature, corresponding to a viscosity of 28 Pa s. On the other hand, the optimal viscosity of AUPPEG8K was between 120 and 140 Pa s. Lower temperatures resulted in a too high viscosity (approximately 260 Pa s for AUPPEG8K at 60 °C), leading to inadequate polymer extrusion for 3D printing. For AUPPEG8K, a temperature of 80 °C was selected as the final printing temperature, corresponding to a viscosity of 136 Pa s. The optimal viscosity ranges of AUPPEG4K and AUPPEG8K show similar viscosity values compared to previously reported PEG-modified epoxy acrylate systems (20–200 Pa s).[59] As expected, the viscosity of AUP melts increased with an increase in molar mass due to more chain entanglements. Given the molar mass related differences in melt viscosities for AUPPEG4K and AUPPEG8K, printing needle diameters of 200 μm (G27) and 250 μm (G25) were used, respectively.

With the printing temperature and the needle diameter defined, we varied the printing pressure in the range of 1–5 bar, while keeping all other parameters constant. At pressures lower than 3 bar, the material flow, particularly for AUPPEG8K, was insufficient to enable printing. In addition, at pressures higher than 5 bar, the excess material flow, especially for AUPPEG4K, was too high, resulting in strut diameters that were 200 μm larger than anticipated. Therefore, the pressure range for printing was set between 3 and 5 bar for both AUPs.

3.2.2. Determination of the printing speed range. In the next step, within the defined pressure range, we studied the effect of the printing speed (100–800 mm min^{-1}) on the strut diameter and the layer thickness of the scaffolds for printing pressures of 3 or 5 bar. The results are shown in Table 2. The strut diameter and the layer thickness of the scaffolds were correlated with the printing pressure and speed. A higher printing pressure, which implies a higher amount of polymer extruded from the print head, resulted in an increase in polymer flow, leading to larger strut diameters and thus, thicker layers. In contrast, increasing the printing speed implies a shorter time for polymer deposition, resulting in a decrease in polymer flow, indicating thinner strut diameters and layers. An increase in printing pressure and speed thus has opposite effects on the strut diameter and the layer thickness.

Within the defined printing speed range (between 100 mm min^{-1} and 800 mm min^{-1}), a non-uniform strut pattern was observed for AUPPEG4K at printing speeds lower than 250 mm min^{-1} (data not shown) due to the longer polymer deposition time, which resulted in larger strut diameters than the selected

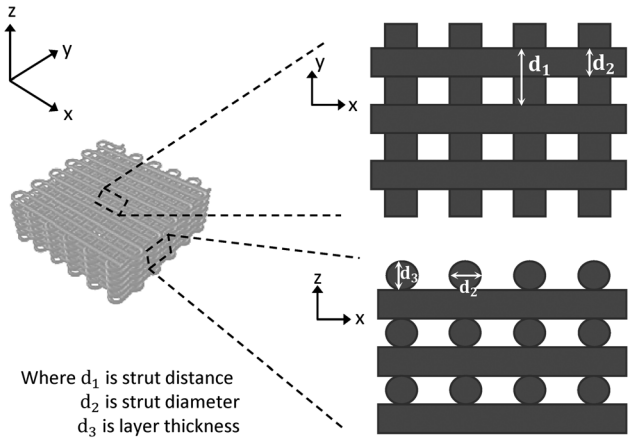

Fig. 2 Applied 3D model of porous AUP scaffolds. The top right image represents the scaffold top view while the bottom right image represents the side view/cross-section of the scaffold.

 This journal is © The Royal Society of Chemistry 2026

Open Access Article. Published on 21 January 2026. Downloaded on 5/27/2026 2:20:44 AM. This article is licensed under a Creative Commons Attribution-NonCommercial 3.0 Unported Licence.

Table 2 Effect of 3D printing speed and pressure on the scaffold strut diameter, the pore size, the layer thickness and the aspect ratio (n) for AUPPEG4K and AUPPEG8K

Material	*XY*-printing speed (mm min^{-1})	Pressure (bar)	Strut diameter (μm)	Pore size (μm)	Layer thickness (mm)	$n = \frac{d_3}{d_2}$	p values[a]
AUPPEG4K	250	3	370 ± 14	227 ± 18	0.11	0.30	0.066
AUPPEG4K	250	5	400 ± 30	204 ± 14	0.12	0.30	7.51×10^{-9}
AUPPEG4K	500	3	200 ± 60	396 ± 10	0.11	0.55	1.31×10^{-6}
AUPPEG4K	500	5	230 ± 25	367 ± 11	0.13	0.57	0.071
AUPPEG8K	250	3	220 ± 45	382 ± 15	0.13	0.59	0.054
AUPPEG8K	250	5	260 ± 40	344 ± 17	0.14	0.54	0.08
AUPPEG8K	500	3	210 ± 35	388 ± 14	0.13	0.62	0.42
AUPPEG8K	500	5	240 ± 30	357 ± 13	0.13	0.54	0.12

[a] p values are based on strut diameter differences. The p values on the first, second, third and fourth rows represent the significant differences between 3 and 5 bar at 250 mm min^{-1}, 250 and 500 mm min^{-1} at 5 bar, 250 and 500 mm min^{-1} at 3 bar, and 3 and 5 bar at 500 mm min^{-1}, respectively. The identical comparison is valid for AUPPEG8K.

needle diameter. On the other hand, a decrease in material outflow was observed at printing speeds higher than 500 mm min^{-1} due to the shorter polymer deposition time. This resulted in smaller strut diameters than the selected needle diameter, irrespective of the AUP type and the applied printing pressure. Therefore, in what follows, printing speeds of 250 and 500 mm min^{-1} were chosen as the limits for both AUPs to study the optimal combination(s) of printing speed and pressure.

3.2.3. Determination of the optimal combination of the printing speed and pressure. The results of the obtained strut diameters, pore sizes, layer thicknesses and the aspect ratios (*i.e.* n) of struts for each of the investigated combinations of printing speed and pressure for both types of AUP are shown in Table 2. The aspect ratio of the struts (n) can be derived from the ratio of d_3 to d_2 (Fig. 2 and Fig. S12).

When comparing the obtained strut diameters (obtained from the scaffold top view) and the layer thicknesses (obtained by dividing the scaffold height by the number of printed layers) for all printed scaffolds (ranging between 110 and 140 μm, Table 2), it becomes evident that the printed struts are not cylinder but ellipsoid-shaped, irrespective of the applied combination of printing pressure and speed (Fig. S12). The finding of non-cylindrical shaped polymer struts is consistent with data for previously reported soft elastomers, including polycarbonate-based silicone (PCU-Sil)[60] and modified gelatin containing hydrogels.[61] In contrast, more rigid materials such as PLLA, PLGA and PCL typically yield cylindrical polymer struts.[62,63] Non-cylindrical struts can be attributed to a time-dependent stress-relaxation phenomenon known as extrudate swell in viscoelastic polymers. This is due to the elastic strain energy stored in the polymer melt during the extrusion within the nozzle. Upon leaving the nozzle, the stored elastic energy can only relax when the polymer chains reorient and return to their state prior to extrusion, resulting in contraction in the flow direction and thus, an expansion in the strut diameter.[64–66]

Printing parameters that produce a low and a high material outflow were compared to determine the strut diameter range that can be obtained for AUPPEG4K scaffolds. While printing parameters of 250 mm min^{-1} and 5 bar gave the highest material outflow, resulting in struts with a diameter of 400 ± 30 μm, printing parameters of 500 mm min^{-1} and 3 bar provided the lowest material outflow, resulting in struts with a diameter of 200 ± 60 μm. Despite the fact that the latter combination of printing speed and pressure resulted in a perfect match between the printed strut diameter and the selected 200 μm needle diameter, it also revealed the highest standard deviation. Looking at the other applied combinations of printing speed and pressure (see Table 2), struts with a diameter of 230 ± 25 μm or 370 ± 14 μm were obtained. This implies that by varying the printing parameters, the development of AUPPEG4K scaffolds with strut diameters in the range of 200–400 μm is feasible.

When comparing the data, the effect of the printing speed on the strut diameter of AUPPEG4K scaffolds was more prominent than the effect of the pressure (Fig. 3 and Table 2). Indeed, the change in printing speed while keeping the

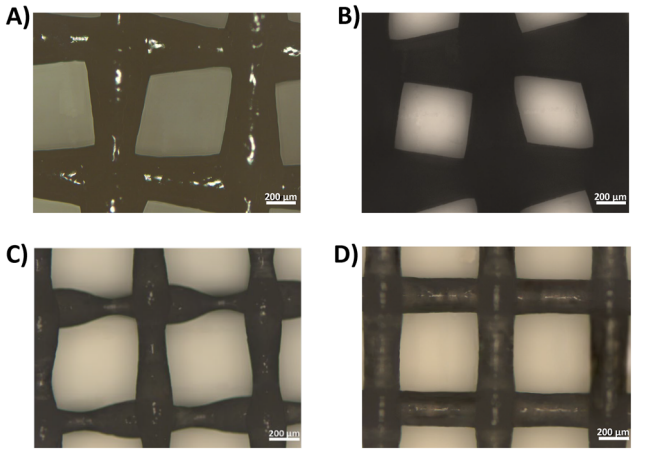

Fig. 3 Optical microscopy images of deposited layers of AUPPEG4K scaffolds from the top view. (A) Scaffold obtained with a printing speed of 250 mm min^{-1} and a pressure of 3 bar. (B) Scaffold obtained with a printing speed of 250 mm min^{-1} and a pressure of 5 bar. (C) Scaffold obtained with a printing speed of 500 mm min^{-1} and a pressure of 3 bar. (D) Scaffold obtained with a printing speed of 500 mm min^{-1} and a pressure of 5 bar. Scale bar is 200 μm.

Open Access Article. Published on 21 January 2026. Downloaded on 5/27/2026 2:20:44 AM.
This article is licensed under a Creative Commons Attribution-NonCommercial 3.0 Unported Licence.

pressure constant affected the strut diameter more than a change in pressure when keeping the printing speed constant. More specifically, strut diameters obtained at 250 mm min^{-1} significantly differed from those obtained at 500 mm min^{-1} while keeping the pressure constant (both $p < 0.05$ for the 3 bar and the 5 bar cases). However, the obtained strut diameters when keeping the printing speed constant with a change in pressure were not significantly different (both $p > 0.05$). Optical microscopy images from the AUPPEG4K scaffolds revealed that a non-uniform strut pattern was observed during printing with a higher printing speed and a lower printing pressure (500 mm min^{-1} and 3 bar, Fig. 3C). Increasing the printing pressure from 3 to 5 bar improved the uniformity of the struts (Fig. 3C *versus* Fig. 3D). A similar effect of increased pressure on the uniformity of the strut diameters was not evident for scaffolds obtained by applying a printing speed of 250 mm min^{-1} (Fig. 3A *versus* Fig. 3B). Considering the effect of the 3D printing speed and pressure on the strut diameter of AUPPEG4K scaffolds, the printing parameters of 250 mm min^{-1}, 3 bar (Fig. 3A and Table 2) and 500 mm min^{-1}, 5 bar (Fig. 3D and Table 2) resulted in the scaffolds with the most uniform struts. Therefore, these printing parameters formed the base for the continuation of our study.

For the scaffolds based on AUPPEG8K, a completely different picture was observed. Given the higher viscosity of AUPPEG8K melts compared to their AUPPEG4K counterparts (see higher: 136 *versus* 28 Pa s), the material outflow of the former was lower. As a result, both the printing speed and pressure had no significant effect (both $p > 0.05$) on the strut diameters (Table 2 and Fig. S9). A printing pressure of 5 bar combined with printing speeds of 250 or 500 mm min^{-1} both gave an almost perfect match with the applied needle diameter (250 μm). Indeed, both printing speeds yielded scaffolds with strut diameters of 260 ± 40 μm and 240 ± 30 μm, respectively, closely matching the applied needle diameter. Another outcome of the lower material outflow due to the higher viscosity of AUPPEG8K was the more cylindrical nature of the obtained struts, as reflected by the larger n values for the AUPPEG8K scaffolds as compared to their AUPPEG4K counterparts (Table 2). Finally, when looking at the obtained pore sizes (Table 2), it was obvious that given the ellipsoidal shape of the printed struts, the pore sizes decreased with an increasing strut diameter for both AUPPEG4K and AUPPEG8K.

When summarizing all the obtained data, it can be concluded that for AUPPEG4K, the printing speed and/or pressure variation enables control over the scaffold strut diameter and pore size. For the AUPPEG8K material, no control can be realized, as evidenced by the non-significant differences (p: 0.05 and 0.08) obtained, at least in the studied condition range. The differences between both AUPs can be ascribed to the differences in viscosity between both melts. In case future research indicates the necessity to develop AUPPEG8K scaffolds with different morphologies, printing needles with a larger diameter (*e.g.*, G23) will be applied. For the continuation of the present research, our work will focus on AUPPEG4K, while using AUPPEG8K as a comparative material.

To the best of our knowledge, this is the first report ever on printing PEO-based hydrogel building blocks from the melt *via* extrusion-based 3D printing. For benchmarking purposes, we compared our materials with PEO6K-DA, a commercially available hydrogel building block containing a PEO with a molar mass of 6000 g mol^{-1} (M_n) and one acrylate functional group at each chain end. This material comes close to the herein developed hydrogel building blocks in terms of both molar mass and chemical composition. The viscosities for PEO6K-DA at 57 °C with and without the photoinitiator (PI, 2 mol% Irgacure 2959 relative to the acrylates) are 2.66 Pa s and 6.67 Pa s, respectively. Thus, the viscosities are too low to enable extrusion-based melt printing. Furthermore, the commercial PEO6K-DA hydrogel building block does not reveal the typical shear-thinning behavior, in which fluid viscosity decreases with increasing shear, of the AUP materials.

3.2.4. Printing of AUP scaffolds with varying pore sizes and strut diameters. Based on available literature data, the optimal pore size range of a meniscal scaffold (at least for a partial meniscectomy) must be between 150 and 500 μm to enable meniscal tissue infiltration.[27,67,68] Using the above-reported optimized printing parameters (printing at speeds of 250 mm min^{-1} and a pressure of 3 bar *versus* 500 mm min^{-1} and a pressure of 5 bar) and considering the optimal pore size range, this study aimed to print scaffolds with three different pore sizes (220, 370, and 520 μm) and two different strut diameters (230 and 370 μm). The computer-aided design (CAD) models for the scaffolds, together with representative optical microscopy images of a selection of the obtained AUPPEG4K scaffolds (dry and swollen), are shown in Fig. 4. The optical microscopy images of AUPPEG8K scaffolds (dry and swollen) are shown in Fig. S10 as a reference.

Data were extracted using the images from the dry as-printed scaffolds to compare the theoretical and experimental pore sizes (Fig. 5A). The results revealed that for both strut diameters studied, there was a linear correlation between the theoretical and experimental pore sizes ($R^2 = 1.0$ for both strut diameters). Thus, these data indicated that scaffolds with varying pore sizes can be printed reproducibly (standard deviation of 2.0–6.4% corresponding to 10–30 μm). Furthermore, irrespective of the selected strut diameter and the theoretical pore size, the experimental pore sizes were lower compared to the theoretical ones (difference ranging from 5.1–13.3% for AUPPEG4K scaffolds). This can be explained by the ellipsoidal shape of the obtained struts (previously described). Correction for this deviation is possible by adapting the scaffold design. Moreover, a comparison of the resemblance between the theoretical pore size (as designed) and the experimental pore size of the AUPPEG8K scaffolds revealed differences ranging from 2% to 10% (Table 2), depending on the exact printing parameters (polymer and device). AUPPEG4K scaffolds thus have a lower CAD/CAM mimicry compared to AUPPEG8K scaffolds, yet this can be attributed to the lower viscosity of the AUPPEG4K melt compared to the AUPPEG8K melt. The obtained values matched with the literature for scaffolds 3D printed from PGA and PLA,[69,70] even though CAD-CAM

 This journal is © The Royal Society of Chemistry 2026

Open Access Article. Published on 21 January 2026. Downloaded on 5/27/2026 2:20:44 AM.
This article is licensed under a Creative Commons Attribution-NonCommercial 3.0 Unported Licence.

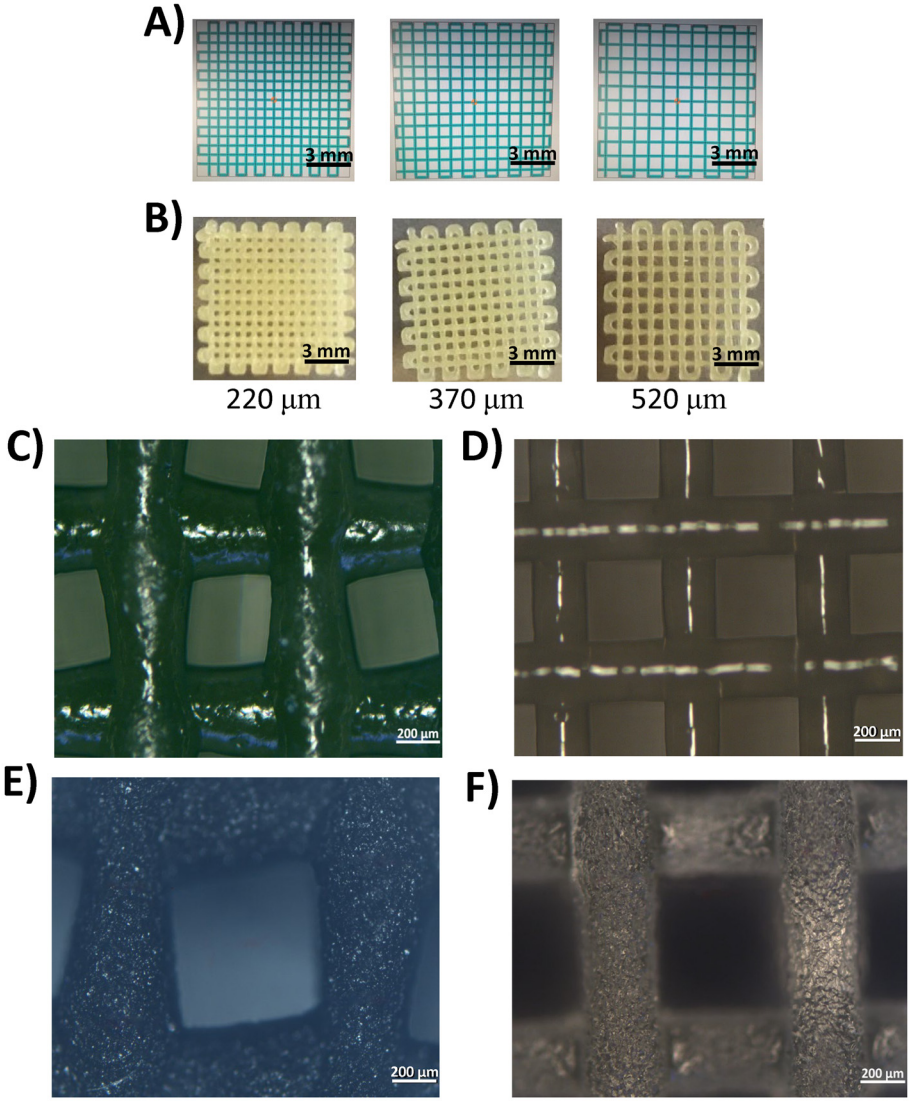

Fig. 4 Optical characterization of AUPPEG4K scaffolds. (A) CAD model of the printed scaffolds. (B) Macroscopic images of as-printed AUPPEG4K scaffolds with different pore sizes (PS). (C–F) Optical microscopy images of scaffolds. (C) AUPPEG4K scaffold with 370 µm PS and 370 µm struts (printed with 250 mm min^{-1} and 3 bar). (D) AUPPEG4K scaffold with 370 µm PS and 230 µm struts (printed with 500 mm min^{-1} and 5 bar). (E) Swollen state of the scaffold depicted in panel (C). (F) Swollen state of the scaffold depicted in panel (D). Scale bars are 3 mm and 200 µm for (A), (B) and (C–F), respectively.

mimicry was lower for 3D printed modified gelatin hydrogels with a difference of 25%.[71]

For the anticipated biomedical application, the scaffolds will be present under water-swollen conditions. To this extent, knowledge of the pore sizes in the hydrated state is of paramount importance. Fig. 5B shows the correlation between the pore sizes in the dry and hydrated states. Upon incubation in water, the scaffolds swelled and as a result, the diameter of the struts and the pore size increased. For the AUPPEG4K scaffolds, there was a linear correlation between the pore size in the dry and the hydrated state, irrespective of the strut diameter (R^2 of 0.98 and 0.97 for strut diameters of 230 µm and 370 µm, respectively). Based on these correlations, the experimental pore size of scaffolds in the swollen state can be extrapolated for a specified set of printing parameters (including printing speed and pressure).

Fig. 5 also shows that scaffolds with smaller struts (230 µm) swelled more compared to their larger diameter counterparts. This finding can be explained by the fact that in one unit volume, a larger number of pores and polymer struts were present for the scaffolds with smaller diameter struts. This led to a more pronounced swelling, given the larger available polymer surface area for water contact. Moreover, a final observation is that the scaffold swelling originated more from a pore size increase than an increase in strut diameter (Fig. 4C–F). As an example, for the AUPPEG4K scaffolds, the pore sizes for the 370 µm diameter struts increased from 220, 370, and 520 µm to 350, 600 and 725 µm, respectively, whereas the strut dia-

Open Access Article. Published on 21 January 2026. Downloaded on 5/27/2026 2:20:44 AM.
This article is licensed under a Creative Commons Attribution-NonCommercial 3.0 Unported Licence.

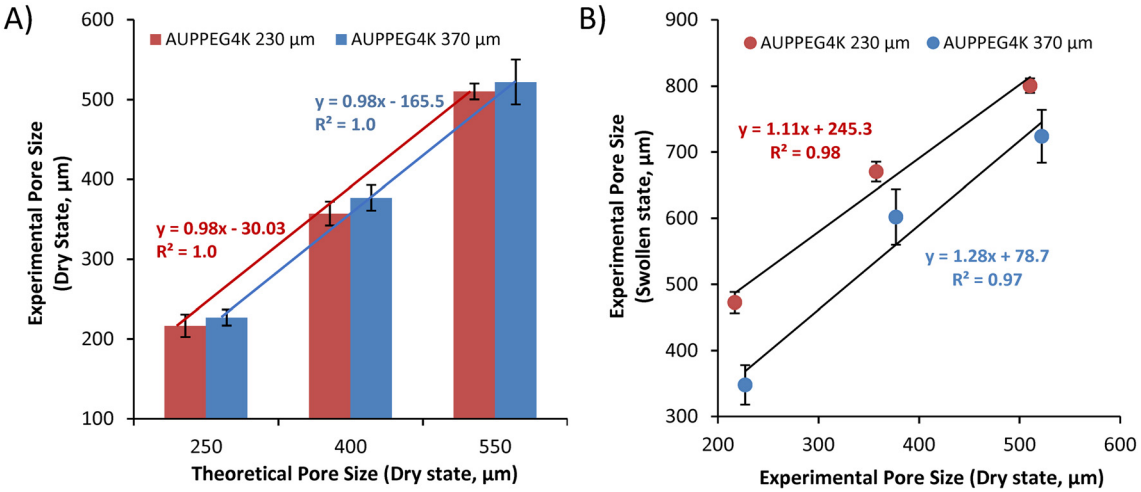

Fig. 5 Pore size correlations of AUPPEG4K scaffolds obtained *via* optical microscopy. (A) Theoretical pore size *versus* experimental pore size for dry scaffolds. (B) Experimental pore size of scaffolds in the dry *versus* hydrated state.

meters increased to 475, 485 and 495 µm. The correlations between the pore sizes in the dry and hydrated state for AUPPEG8K scaffolds are shown in Fig. S11. The observed correlations for AUPPEG8K were similar to those for AUPPEG4K, while being more extended for AUPPEG8K, given the higher molar mass of the building block, thus leading to a higher swelling.

In addition to optical microscopy of the printed scaffolds used for optimizing various printing-related parameters, we selected one scaffold (AUPPEG4K, printing speed 250 mm min^{-1}, printing pressure 3 bar) for nano-CT analysis. The aim was a visualization of the entire 3D scaffold (scaffold contours and bulk), while horizontal and vertical cross-sections could prove the interconnected porous structure and enable porosity determination. The results are shown in Fig. 6.

Top views of the dry and water-swollen scaffolds are shown in Fig. 6B and C. From these, pore size and strut diameter of 320 and 400 µm, respectively, can be derived for the dry scaffolds. These values confirmed the data from optical microscopy (*cf.* pore size and strut diameter of 350 and 370 µm, respectively). A comparison of dry and swollen scaffolds (Fig. 6C and D) indicates that the scaffolds expanded 1.5-fold in 3D in all (x, y, z) directions. In addition, the nano-CT based finding of the 1.5-fold scaffold expansion from dry to hydrated state can be corroborated with optical microscopy images (Fig. 4C and E) based on the comparison of the strut distance in dry and hydrated states.

The interconnected nature of pores in the developed scaffold, both in the dry and hydrated states, can be seen in Fig. 6D. The interconnected porous nature of the AUPPEG4K scaffold can also be confirmed *via* the cross-sections at different levels and angles (Fig. S13). From this 3D reconstruction, porosities of 44% and 36% were calculated for the dry and hydrated scaffolds, respectively. These porosity values are in the same range as the porosity findings of human menisci by Zhu *et al.*, where the mean porosity of the human meniscus

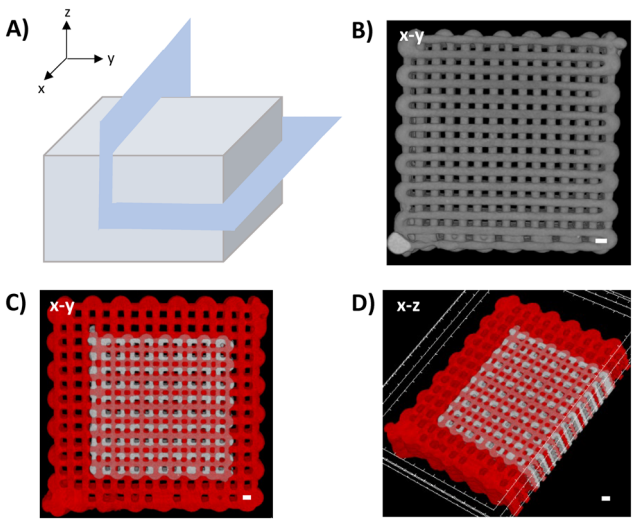

Fig. 6 Nano-CT analysis of AUPPEG4K scaffolds with 350 µm pore size and 370 µm strut diameter. (A) Schematic depiction of the scaffold cross-section. (B and C) Top view images (x–y plane) of scaffolds; grey and red represent the dry and swollen state of the scaffold, respectively. (D) Perspective view images of the scaffolds depicted in panel (C). Scale bar is 500 µm.

was 34%.[72] This finding implies that the selected scaffold designs can be effective candidates for meniscus tissue engineering. In contrast, the results obtained by Pereira *et al.* showed that the mean porosity of human meniscus based on micro-CT was 55% for a freeze-dried lateral meniscus.[73] Yet, the observed difference in the literature might have been caused by the applied sample preparation and analysis methods.

For the dry scaffolds, the obtained data from nano-CT was 10% lower than the theoretical value calculated using eqn (1), as reported earlier.[39,40] Based on this theoretical approach, the

This journal is © The Royal Society of Chemistry 2026

Open Access Article. Published on 21 January 2026. Downloaded on 5/27/2026 2:20:44 AM.
This article is licensed under a Creative Commons Attribution-NonCommercial 3.0 Unported Licence.

porosities of all other developed scaffolds in the dry state were calculated. The porosities varied between 48% and 74% depending on the pore sizes, the strut diameters, and the layer thicknesses. The porosities obtained in our work are in the range of earlier studies in the field of meniscus TE. Indeed, for PGA scaffolds with a 0–90° lay-down pattern, 350 μm struts, and 200–500 μm pore sizes, the obtained porosities were 52–68%.[69,74] Considering the comparison of the experimental and theoretical porosity, the experimental porosity of scaffolds can thus be extrapolated for a specified set of strut diameters, strut distances and layer thicknesses.

3.3. Physicochemical characterization of 3D printed AUP scaffolds

3.3.1. Gel fraction and swelling of scaffolds. In the next part of our work, the developed scaffolds with varying strut diameters and pore sizes, photocrosslinked with and without PI, were tested for their gel fraction and swelling properties.

The data for AUPPEG4K, shown in Fig. 7, reveal some major findings. For all scaffolds, gel fractions in the range of 64–89% were obtained. Furthermore, the obtained gel fractions were higher for scaffolds with larger strut diameters (74–89% for 370 μm diameter scaffolds *versus* 64–80% for 230 μm diameter scaffolds). As the gel fraction of the scaffolds indicates the amount of polymer covalently crosslinked in the network, a higher gel fraction thus implies a higher network density. All gel fractions were above 70%, which indicates that the scaffolds were efficiently crosslinked and will retain their integrity and strength.[75] The only exception was the scaffolds with the smallest pore size and strut diameter crosslinked in the absence of a PI. The obtained data indicate that an acrylate content in the AUPPEG4K melt (Table 1, *i.e.* 0.33 mmol acrylate per g AUP) is sufficient to realize efficient post-printing crosslinking.

The fact that all gel fractions were lower than 100% and higher for scaffolds with thicker struts may be attributed to

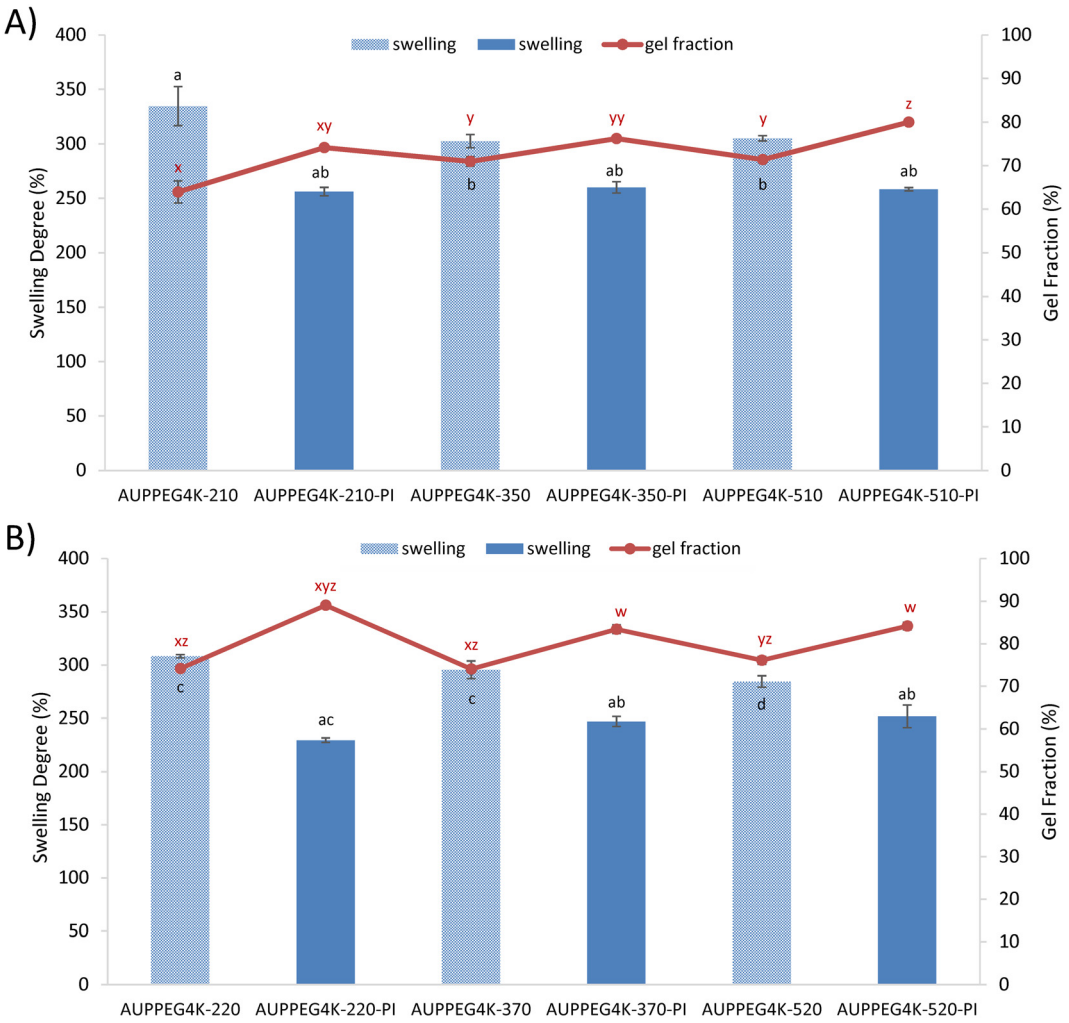

Fig. 7 The effect of the strut diameter and pore size on the swelling degree and gel fraction of AUPPEG4K scaffolds. (A) Scaffolds with 230 μm struts. Patterned and solid fill represent the absence and presence of PI in the AUPs, respectively. (B) Scaffolds with 370 μm struts. Bars labeled with the same letter (a, b, c) are not significantly different; lines labeled with the same letter (w, x, y, z) are not significantly different ($p > 0.05$). Statistically significant difference, $n = 3$, $p < 0.05$.

Open Access Article. Published on 21 January 2026. Downloaded on 5/27/2026 2:20:44 AM.
This article is licensed under a Creative Commons Attribution-NonCommercial 3.0 Unported Licence.

the selected crosslinking method. Indeed, the applied UV light can be scattered on the struts of the polymer scaffolds. This decreases the penetration depth and/or the intensity of the UV light, which negatively affects the efficiency of the crosslinking reaction in the central part of the scaffold. As scaffolds with thinner struts possessed a larger surface area, the scattering was more pronounced, thus causing a lower gel fraction than scaffolds with larger diameter struts. We also observed that the obtained gel fractions increased significantly by 5–15% upon PI addition. As indicated in the introduction section, one of the unique features of the herein reported AUP macromonomers is the fact that they are crosslinkable in the absence of a PI. However, the presence of 2 mol% PI indicates a higher crosslinking efficiency for the scaffolds, leading to higher gel fractions (above 80%). At 4 mol%, no further increase was observed for AUPPEG4K scaffolds. The effects of the PI concentration on the gel fraction and the swelling properties of AUPPEG8K scaffolds are shown in Fig. S14. The optimal PI concentration was 4 mol%. Although the selected PI concentrations were 2 and 4 mol% for AUPPEG4K and AUPPEG8K, the scaffolds without PI were also investigated and used as a benchmark for observing the positive effect of PI presence on the gel fractions.

The obtained swelling data corroborate the gel fraction results. The swelling degree of all AUPPEG4K scaffolds ranged between 250% and 350% (Fig. 7), implying that the scaffolds took up an amount of water that is 2.5 to 3.5 times their dry weight. The swelling degrees of AUPPEG8K scaffolds, ranging between 460% and 530%, are shown in Fig. S14. As anticipated, the swelling thus increases with increasing PEG molar mass (*cf.* leading to a lower crosslinking density). Similarly, a study conducted by Nguyen *et al.* on PEG diacrylate (PEGDA) hydrogel sheets (PEG molar mass of 6000 and 10 000 g mol^{-1}) showed the effect of PEG molar mass and the concentration (10–30 wt%) on the swelling properties. As the molar mass of PEG increased from 6k to 10k with a 30 wt% concentration, hydrogels exhibited an increase in swelling ratio from 7.4 to 14.6.[76] The higher water uptake in their study can be attributed to the lower PEG concentrations compared to the AUP polymer melts (100 wt%) applied in our study. From the data, it can also be concluded that the addition of PI negatively and significantly affects the swelling degree, irrespective of the investigated strut diameter and pore size. This finding is associated with the higher crosslinking densities obtained upon PI addition (*cf.* gel fraction data). Finally, we showed that both the pore size and the strut diameter of the developed scaffolds do not affect the swelling degree, at least in the investigated ranges of the pore size (200 μm to 500 μm) and the strut diameter (230 and 370 μm).

3.3.2 Mechanical properties of AUP scaffolds in the hydrated state. Subsequent to analyzing the physical properties of AUP scaffolds, the characterized AUP scaffolds were further investigated by uniaxial unconfined compression tests to determine their mechanical properties, including the compressive strength, the deformation at break and the compressive modulus. Although the selected PI concentrations were 2% and 4 mol% for AUPPEG4K and AUPPEG8K, respectively, the scaffolds without PI were used as a benchmark for observing possible effects on the mechanical properties of the scaffolds. As a meniscal substitute candidate, the AUP scaffolds were analyzed in the hydrated state, as in the final application.

A series of important findings can be derived from the data summarized in Fig. 8 for AUPPEG4K scaffolds with strut diameters of 230 and 370 μm, respectively. Firstly, scaffolds with a larger strut diameter revealed higher compressive strengths, deformations at break and compressive moduli. As anticipated, the scaffolds with 370 μm struts were more robust than their 230 μm strut diameter counterparts. Secondly, the addition of PI positively affected all the mechanical properties studied, irrespective of the strut diameter or pore size. This can be explained by the increase in gel fraction of the crosslinked hydrogel network upon PI addition (see section 3.3.1) and confirms data from the literature using photo-crosslinkable gelatin and chitosan hydrogel building blocks.[77,78]

Thirdly, for both strut diameters studied, an increasing pore size led to a decrease in compressive strength, deformation at break and compressive moduli. As the pore size of the scaffold increases, the number of polymer struts (*i.e.* the amount of AUP present) in one unit volume of the scaffold decreases, thus causing a lower resistance towards the applied stress, resulting in a decrease in the mechanical properties. From the data obtained, it can thus be concluded that the addition of PI and an increase in pore size have opposing effects on the compressive moduli of the scaffolds. This finding is in agreement with the literature, where the mechanical properties of 3D printed scaffolds decrease with increasing pore size for PCL, PLA-based and poly(ethylene oxide terephthalate)-poly(butylene terephthalate) (PEOT-PBT) block copolymers.[39,79,80] In addition, there was a positive correlation between the compressive strength and the deformation at break, irrespective of the investigated strut diameter and pore size. This can be explained by the fact that scaffolds with higher compressive strength can withstand the applied mechanical loading more, leading to higher deformation until they reach failure.

However, a few exceptions were observed in the decreasing trend of the mechanical properties while increasing the pore size. In particular, in the absence of PI, the compressive moduli of scaffolds with 230 μm struts (Fig. 8C) were independent ($p = 0.25$) of the pore size increase, at least in the studied pore size range. This could be attributed to the predominating effect of the lower gel fraction (64–71%, Fig. 7A) of these scaffolds, which ruled out the effect of the pore size on the compressive modulus. Another exception from the general trend was the scaffolds with 370 μm struts printed in the presence of PI (Fig. 8F). This finding can be due to the profound effect of the gel fraction (83–89%) on the mechanical properties upon PI addition. This effect counterbalances the anticipated decreasing tendency of the compressive modulus with pore size increase ($p = 0.05$). For these exceptions, it can be concluded that the effect of the gel fraction on the compres-

 This journal is © The Royal Society of Chemistry 2026

Open Access Article. Published on 21 January 2026. Downloaded on 5/27/2026 2:20:44 AM.
This article is licensed under a Creative Commons Attribution-NonCommercial 3.0 Unported Licence.

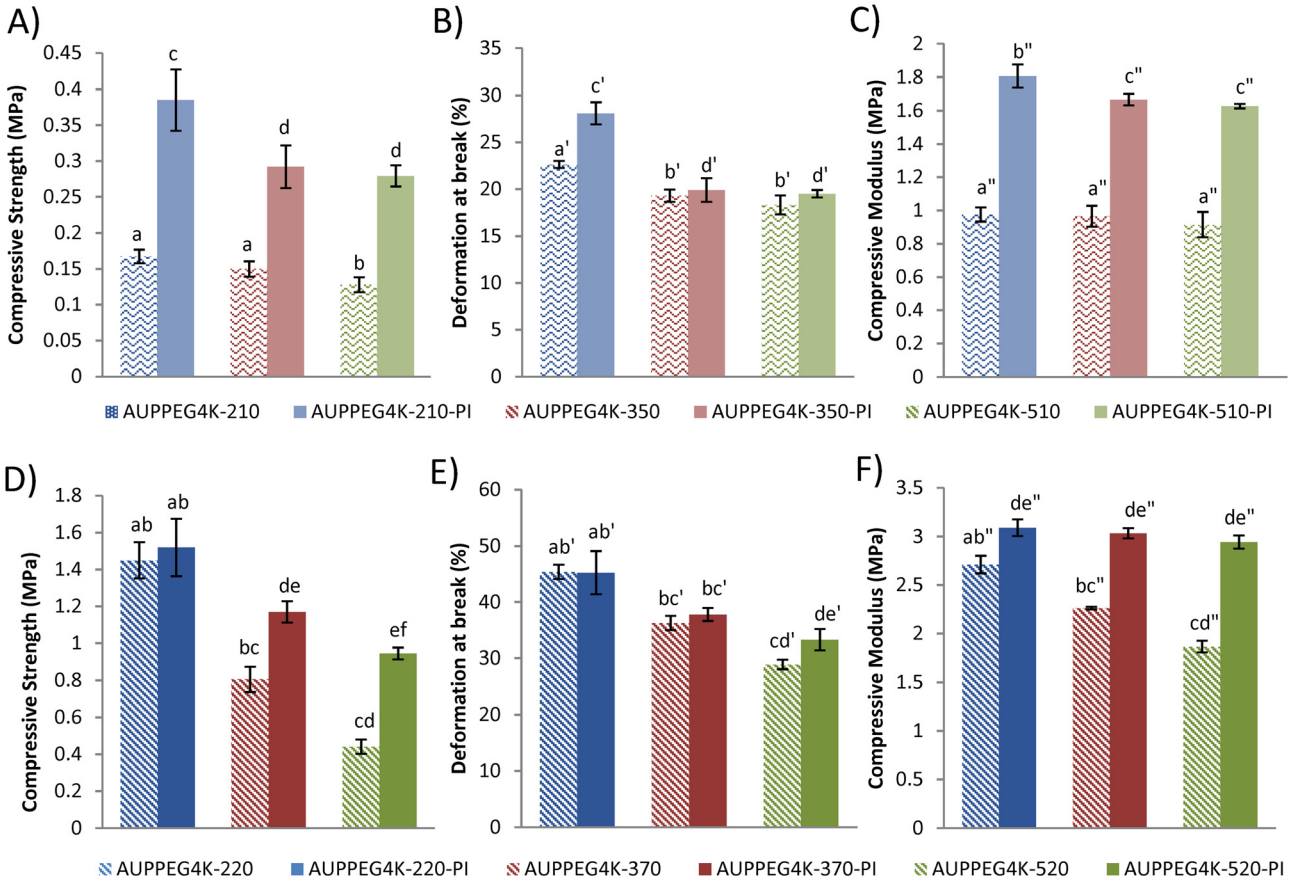

Fig. 8 Effect of pore size and PI on the mechanical properties of AUPPEG4K scaffolds. (A) Compressive strength of scaffolds with 230 μm struts. (B) Deformation at break of scaffolds with 230 μm struts. (C) Compressive modulus of scaffolds with 230 μm struts. (D) Compressive strength of scaffolds with 370 μm struts. (E) Deformation at break of scaffolds with 370 μm struts. (F) Compressive modulus of scaffolds with 370 μm struts. PI indicates the presence of 2 mol% Irgacure 2959 relative to the acrylates present in AUPPEG4K. Bars labeled with the same letter (a, b, c) are not significantly different. Statistically significant difference, $n = 3$, $p < 0.05$.

sive modulus is more prominent than the effect of the pore size, at least in the studied pore size range.

A final observation was a leveling off of the compressive strength and the deformation at break values for the lower strut diameter scaffolds (*i.e.* 230 μm, Fig. 8A and B). A possible explanation for this might be that the pore size effect was counterbalanced by the effect of the gel fractions (Fig. 7A).

For comparative reasons, a limited set of data from AUPPEG8K scaffolds with 230 μm strut diameters and pore sizes of 350 and 510 μm are shown in Fig. S15. As expected, AUPPEG8K scaffolds revealed lower mechanical properties, as reflected by both the compressive strength and the modulus. In particular, 2.5- and 3-fold decreases were observed for AUPPEG8K scaffolds with 350 and 510 μm pore sizes, respectively, compared to their AUPPEG4K counterparts. This can be explained by the lower crosslink density of the AUPPEG8K scaffolds, resulting in higher flexibility, leading to a higher deformation at break in AUPPEG8K scaffolds. Additionally, an increase in pore size from 350 to 510 μm led to a decrease in the mechanical properties of AUPPEG8K scaffolds, as anticipated.

A meniscal scaffold must combine many crucial characteristics, particularly with regard to its mechanical properties. The compressive moduli of the developed AUPPEG4K and 8K scaffolds were in the range of 1–3 MPa and 0.5–0.7 MPa, respectively, under physiological strains, depending on the selected pore size and the strut diameter. In our study, the compressive moduli of the developed scaffolds (0.5–3.2 MPa) were determined as the elastic compressive modulus, calculated from the slope of the stress–strain curve in unconfined compression. Compressive moduli of the human meniscus reported in the literature are in the range of 0.7–5 MPa.[12–15,81] These values are either the elastic compressive modulus from unconfined or confined compression, or the instantaneous modulus from indentation-based stress–relaxation tests. Although obtained through different protocols, both measure the tissue's initial load-bearing stiffness before fluid relaxation and therefore fall in a similar magnitude, typically within 0.1–2 MPa, with higher values up to ~5 MPa observed in the anterior medial region and in the degenerated meniscus. Our scaffolds' moduli are thus in line with the physiologically relevant compressive properties of the native meniscus and out-

Open Access Article. Published on 21 January 2026. Downloaded on 5/27/2026 2:20:44 AM. This article is licensed under a Creative Commons Attribution-NonCommercial 3.0 Unported Licence.

perform those of other reported hydrogel materials. Indeed, different studies on photo-crosslinkable gelatin and PEG-based hydrogel building blocks produced using 3D printing indicated compressive moduli in the kPa range,[82,83] resulting in hydrogel constructs with inferior mechanical properties to those of the native meniscus.

A final part of the mechanical analysis of the developed scaffold involved a nano-CT analysis under mechanical loading. For this test, the AUPPEG4K scaffold that was analyzed for its porosity using nano-CT (printing speed of 250 mm min^{-1}, pressure of 3 bar, 350 μm pore size, and 370 μm strut diameter) was again selected. To mimic the physiological loading conditions in a native meniscus, 10% strain was applied. This value was selected since the meniscus is subject to strain levels ranging from 5% to 15% under physiologically relevant loading conditions, where the typical applied loading procedure includes the dynamic compression under 10% strain.[84–86] The nano-CT data revealed that the morphometric parameters of scaffolds were not significantly affected ($p < 0.05$) upon applying 10% strain (Fig. 9), which is a preliminary indication that the scaffolds can preserve their integrity, structural support, and morphology under physiological mechanical loading.

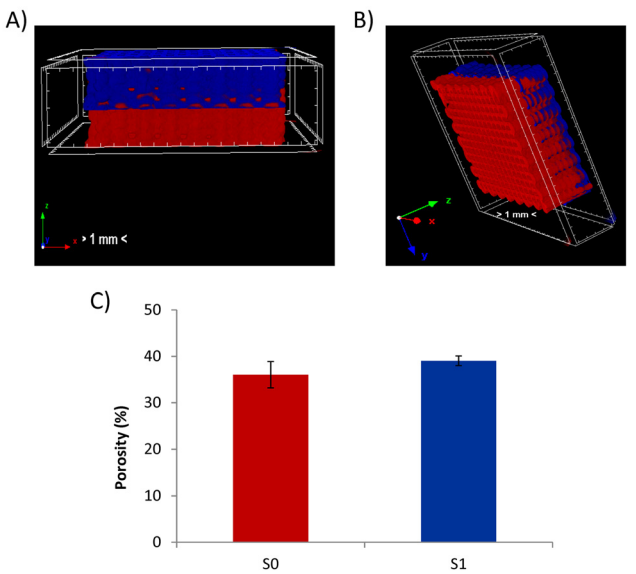

Fig. 9 Nano-CT analysis of AUPPEG4K scaffolds with 370 μm struts and 350 pore size in 2 mol% PI under mechanical loading. Red (S0) is a non-compressed and blue (S1) is a compressed scaffold. (A and B) Side view of the scaffold from different angles. (C) The effect of mechanical loading on the scaffold porosity. S0 and S1 are not significantly different ($n = 3$, $p < 0.05$).

3.4. Surface modification and characterization of AUP scaffolds

With the physical and mechanical evaluation performed, the developed AUP scaffolds were surface-modified using a photo-crosslinkable gelatin derivative (*i.e.* gel-MOD) to introduce a cell-interactive layer on plasma-activated AUP scaffolds. The selected AUPPEG4K scaffold was the same as that applied for the nano-CT analyses (see sections 3.2.4 and 3.3.2). AUPPEG8K is again shown as a reference. The presence of the gel-MOD coating was evaluated by collecting XPS survey scans on both the surface and cross-sections of the scaffolds.

The data shown in Table 3 indicate that on both the AUPPEG4K and 8K scaffolds, no N 1s core-level signal was observed, as no protein (gel-MOD) was present. Upon surface modification using gel-MOD, the increasing N/C ratio was used to demonstrate the covalent link between the gel-MOD and the AUP scaffold surface since the removal of non-reacted gel-MOD was guaranteed by rinsing the surface-modified AUP scaffolds in water at 40 °C (*i.e.* above the upper critical solution temperature (UCST) of gelatin). The data indicate that both the surface and the cross-section of the scaffolds were successfully modified with gel-MOD, considering the presence of N 1s core-level signals. However, the gel-MOD values were different when comparing the surface and cross-section of the AUP scaffolds. A possible explanation can be the lower gel-MOD crosslinking efficiency during UV irradiation on the cross-section because of UV light scattering and limited penetration. Although this difference was significant for AUPPEG4K scaffolds, it was not significantly different for their AUPPEG8K counterparts. These findings could be due to the insufficient immersion time (3 hours) of the AUPPEG4K scaffolds in the gel-MOD solution. This difference can be explained by the higher swelling degree of the AUPPEG8K scaffolds, leading to a larger pore size and resulting in straightforward infiltration of the gel-MOD solution in the entire scaffold compared to their AUPPEG4K counterparts. With the successful gel-MOD immobilization onto AUP scaffolds, the applied gel-MOD coating on the AUPPEG4K scaffold was further evaluated for its distribution over the surface and cross-section of the scaffold *via* XPS

Table 3 Surface compositions and N/C atomic ratios of AUP scaffolds with gel-MOD modification

Material	Location	N (%)	O (%)	C (%)	N/C
AUPPEG4K	Surface	—	32.3 ± 2.8	67.5 ± 2.4	—
AUPPEG4K + gel-MOD	Surface	4.3 ± 1.2	30.3 ± 2.8	65.3 ± 2.6	0.06
AUPPEG4K + gel-MOD	Cross-section	1.7 ± 0.6	30.4 ± 1.2	67.9 ± 1.6	0.02
AUPPEG8K	Surface	—	32.5 ± 2.8	67.5 ± 2.4	—
AUPPEG8K + gel-MOD	Surface	4.1 ± 1.6	29.5 ± 3.3	66.4 ± 2.0	0.06
AUPPEG8K + gel-MOD	Cross-section	3.7 ± 1.7	29.9 ± 1.3	66.3 ± 1.3	0.06
Gel-MOD	Surface	9.1 ± 2.8	22.7 ± 1.3	68.2 ± 1.4	0.13

This journal is © The Royal Society of Chemistry 2026

Open Access Article. Published on 21 January 2026. Downloaded on 5/27/2026 2:20:44 AM.
This article is licensed under a Creative Commons Attribution-NonCommercial 3.0 Unported Licence.

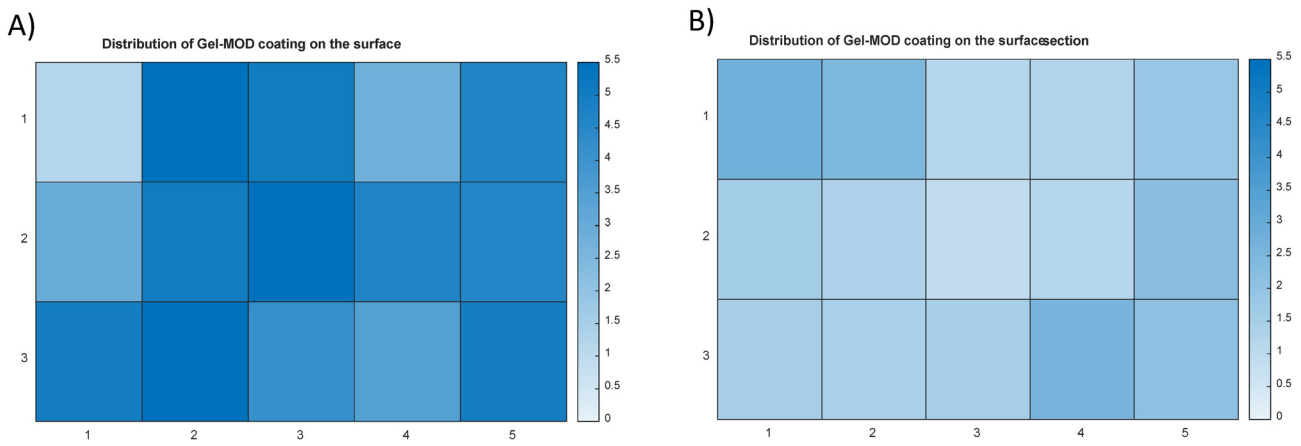

Fig. 10 Distribution of gel-MOD on the AUPPEG4K scaffold. (A) Gel-MOD coating distribution on the scaffold surface. (B) Gel-MOD coating distribution on the scaffold cross-section. The color indicates the % N value.

micro-mapping (Fig. 10), which indicates a homogeneous distribution both on the surface and cross-section of the scaffold.

3.5. *In vitro* cytotoxicity using human dermal fibroblasts

In the final part of this work, the developed AUPPEG4K scaffolds were tested for their *in vitro* cytotoxicity. The selected AUPPEG4K scaffold was the same as that applied for the nano-CT and the surface modification analyses. The *in vitro* biocompatibility of the materials was analyzed in an indirect cytotoxicity assay (Ca-AM/propidium iodide staining and MTT assay) using HDF cells. To this end, HDF cells were exposed to extracts of the studied materials and evaluated after 48 hours. As can be seen in Fig. 11A, the cells have excellent viability and elongated morphology with the extracts of PCL (negative control), AUPPEG4K and gel-MOD coated AUPPEG4K scaffolds. The cells containing the extracts of gel-MOD coated AUPPEG4K scaffolds showed higher cell viability compared to the cells containing the extracts of non-coated AUPPEG4K scaffolds, although this difference was not significant ($p > 0.05$).

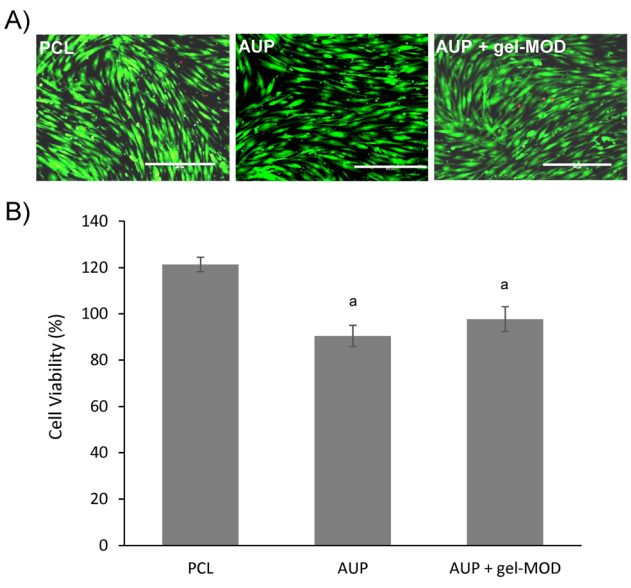

Fig. 11 HDF cell viability using an indirect cytotoxicity assay. (A) Live/dead assay based on Ca-AM/propidium iodide staining. (B) Cell viability based on the MTT assay. Bars labeled with the same letter (a) are not significantly different, $n = 3$. $p < 0.05$. Scale bar is 400 μm.

The cytotoxicity tests showed that the developed AUP does not leach out cytotoxic substances to the cell culture environment. In addition, the morphology of the fibroblasts that were cultured upon incubation in sample extracts from AUP and AUP + gel-MOD media was similar to that of the PCL control group.

Based on these findings, future studies will evaluate the interaction of our scaffolds with meniscal fibrochondrocytes and articular chondrocytes to assess their compatibility with native meniscus and adjacent cartilage tissues, followed by *in vivo* investigations to examine implant integration and functional performance within the joint environment.

4. Conclusion

We successfully synthesized a series of acrylate-terminated urethane-based hydrogel precursors (AUPs). Varying the molar mass of their PEG backbone from 1000 to 8000 g mol^{-1} resulted in AUPs with tunable physicochemical properties. Indeed, going from AUPPEG1K to AUPPEG8K, the acrylate content of the AUPs ranged from 0.81 to 0.16 mmol g^{-1} AUP, the molar masses (M_n) were between 4200 g mol^{-1} and 27 000 g mol^{-1}, the T_c ranged from 10 °C to 36.8 °C, while the T_m ranged between 34.4 °C and 54.6 °C. Considering the solid state crosslinking of AUPs, these polymers were 3D printed from their melts. The optimal combinations of the printing speed and pressure for AUPPEG4K scaffolds (500 mm min^{-1} and 5 bar, 250 mm min^{-1} and 3 bar) resulted in interconnected scaffolds with uniform struts of 230 μm or 370 μm diameter and pore sizes of 220, 370 or 520 μm.

Open Access Article. Published on 21 January 2026. Downloaded on 5/27/2026 2:20:44 AM. This article is licensed under a Creative Commons Attribution-NonCommercial 3.0 Unported Licence.

Almost all gel fractions were above 70%, which implies that the scaffolds were efficiently crosslinked in the solid state and retained their integrity and strength. The scaffold swelling increased with increasing molar mass of the hydrogel building block, while PI addition to scaffolds led to decreased swelling. The mechanical properties of the scaffolds were positively affected by a larger strut diameter, smaller pore sizes and the addition of PI. The compressive moduli of the developed AUPPEG4K and 8K scaffolds were in the range of 1–3 MPa and 0.5–0.7 MPa, respectively, under physiological strains, depending on the selected pore size and the strut diameter. As anticipated, AUPPEG8K scaffolds exhibited lower mechanical properties.

We conclude that the physical properties of the AUP scaffolds can be adjusted by altering the PEG backbone molar mass and varying the processing conditions and the scaffold design. Furthermore, the compressive moduli of AUPPEG4K and AUPPEG8K scaffolds gave promising results considering the mechanical properties of the native meniscus. As the cell viability results indicated that the developed AUP hydrogels were non-toxic, AUPs may fulfill the need in meniscal implant applications given their tunable physical properties, ease in 3D fabrication and biocompatibility.

Conflicts of interest

There are no conflicts to declare.

Data availability

The authors confirm that the data supporting the findings of this article have been included as the supplementary information (SI). Readers interested in the datasets analyzed during the current study can refer to the supplementary information. Supplementary information is available. See DOI: https://doi.org/10.1039/d4bm01730g.

Acknowledgements

Ozge Begum Akalin was partially supported by the 2213/A overseas graduate scholarship program for doctoral training from the Scientific and Technological Research Council of Türkiye (TUBITAK). Peter Dubruel would like to thank the UGent Industrial Research Fund (IOF) for the funding (F2021/IOF-StarTT/071) to execute part of the work. We thank Milena Callies, a master's student at Ghent University, for 3D printing some of the PCL and AUP samples for the *in vitro* cytotoxicity assay. We also acknowledge Sarah Baetens and Elke Berneel from Ghent University Hospital for their significant contributions to the planning and execution of the cell culture experiments. We acknowledge the NMR expertise centre from Ghent University for providing support and access to its NMR infrastructure. The 400 MHz NMR spectrometer used in this work has been funded by a grant of the FWO (grant number I006920N) and the 'Bijzonder Onderzoeksfonds' (BOF) of Ghent University (grant code BOF.BAS.2022.0023.01).

References

1 C. S. Proctor, M. B. Schmidt, R. R. Whipple, M. A. Kelly and V. C. Mow, Material properties of the normal medial bovine meniscus, *J. Orthop. Res.*, 1989, **7**(6), 771–782.
2 J. Sanchez-Adams and K. A. Athanasiou, The knee meniscus: a complex tissue of diverse cells, *Cell. Mol. Bioeng.*, 2009, **2**(3), 332–340.
3 A. J. Fox, A. Bedi and S. A. Rodeo, The basic science of human knee menisci: structure, composition, and function, *Sports Health*, 2012, **4**(4), 340–351.
4 B. W. Leslie, D. L. Gardner, J. A. McGeough and R. S. Moran, Anisotropic response of the human knee joint meniscus to unconfined compression, *Proc. – Inst. Mech. Eng.*, 2000, **214**(6), 631–635.
5 E. E. Williams, J. N. Katz, V. P. Leifer, J. E. Collins, T. Neogi, L. G. Suter, *et al.*, Cost–effectiveness of arthroscopic partial meniscectomy and physical therapy for degenerative meniscal tear, *ACR Open Rheumatol.*, 2022, **4**(10), 853–862.
6 C. C. Scotti, M. T. M. Hirschmann, P. P. Antinolfi, I. Martin and G. Peretti, Meniscus repair and regeneration: review on current methods and research potential, *Eur. Cells Mater.*, 2013, **26**, 150–170.
7 J. Hasan, J. Fisher and E. Ingham, Current strategies in meniscal regeneration, *J. Biomed. Mater. Res., Part B*, 2014, **102**(3), 619–634.
8 C. Jacquet, C. Mouton, R. Becker, H. Koga, M. Ollivier, P. Verdonk, *et al.*, Does practice of meniscus surgery change over time? A report of the 2021 'THE MENISCUS' Webinar, *J. Exp. Orthop.*, 2021, **8**, 46.
9 S. P. Arnoczky and R. F. Warren, Microvasculature of the human meniscus, *Am. J. Sports Med.*, 1982, **10**(2), 90–95.
10 S. A. Maher, S. A. Rodeo, S. B. Doty, R. Brophy, H. Potter, L. F. Foo, *et al.*, Evaluation of a porous polyurethane scaffold in a partial meniscal defect ovine model, *Arthroscopy*, 2010, **26**(11), 1510–1519.
11 C. Van Der Straeten, P. Byttebier, A. Eeckhoudt and J. Victor, Meniscal allograft transplantation does not prevent or delay progression of knee osteoarthritis, *PLoS One*, 2016, **11**(5), e0156183.
12 K. M. Fischenich, K. Boncella, J. T. Lewis, T. S. Bailey and T. L. Haut Donahue, Dynamic compression of human and ovine meniscal tissue compared with a potential thermoplastic elastomer hydrogel replacement, *J. Biomed. Mater. Res., Part A*, 2017, **105**(10), 2722–2728.
13 A. Thambyah, A. Nather and J. Goh, Mechanical properties of articular cartilage covered by the meniscus, *Osteoarthritis Cartilage*, 2006, **14**(6), 580–588.
14 P. Bursac, S. Arnoczky and A. York, Dynamic compressive behavior of human meniscus correlates with its extra-cellular matrix composition, *Biorheology*, 2009, **46**(3), 227–237.
15 I. D. McDermott, S. D. Masouros and A. A. Amis, Biomechanics of the menisci of the knee, *Curr. Orthop.*, 2008, **22**(3), 193–201.

 This journal is © The Royal Society of Chemistry 2026

Open Access Article. Published on 21 January 2026. Downloaded on 5/27/2026 2:20:44 AM. This article is licensed under a Creative Commons Attribution-NonCommercial 3.0 Unported Licence.

16 D. C. Fithian, M. A. Kelly and V. C. Mow, Material properties and structure-function relationships in the menisci, *Clin. Orthop.*, 1990, **252**, 19–31.
17 H. Havıtçıoğlu, R. Özmanevra and A. Karakaşlı, A fibroelastic cartilage: meniscus, in *Musculoskeletal Research and Basic Science*, ed. F. Korkusuz, Springer International Publishing, Cham, 2016, pp. 429–441. DOI: 10.1007/978-3-319-20777-3_25.
18 E. A. Makris, P. Hadidi and K. A. Athanasiou, The knee meniscus: structure-function, pathophysiology, current repair techniques, and prospects for regeneration, *Biomaterials*, 2011, **32**(30), 7411–7431.
19 O. B. Akalin and H. Bayraktar, Alteration of cell motility dynamics through collagen fiber density in photopolymerized polyethylene glycol hydrogels, *Int. J. Biol. Macromol.*, 2020, **157**, 414–423.
20 Z. Z. Zhang, D. Jiang, S. J. Wang, Y. S. Qi, J. X. Ding, J. K. Yu, *et al.*, Scaffolds drive meniscus tissue engineering, *RSC Adv.*, 2015, **5**(95), 77851–77859.
21 W. Niu, W. Guo, S. Han, Y. Zhu, S. Liu and Q. Guo, Cell-based strategies for meniscus tissue engineering, *Stem Cells Int.*, 2016, **2016**(4717184), 10.
22 T. Trzeciak, M. Richter, W. Suchorska, E. Augustyniak, M. Lach, M. Kaczmarek, *et al.*, Application of cell and biomaterial-based tissue engineering methods in the treatment of cartilage, menisci and ligament injuries, *Int. Orthop.*, 2016, **40**(3), 615–624.
23 S. Doppalapudi, A. Jain, W. Khan and A. J. Domb, Biodegradable polymers-an overview, *Polym. Adv. Technol.*, 2014, **25**(5), 427–435.
24 C. K. Kuo, J. E. Marturano and R. S. Tuan, Novel strategies in tendon and ligament tissue engineering: advanced biomaterials and regeneration motifs, *BMC Sports Sci. Med. Rehabil.*, 2010, **2**, 20.
25 J. H. De Groot, H. W. Kuijper and A. J. Pennings, A novel method for fabrication of biodegradable scaffolds with high compression moduli, *J. Mater. Sci. Mater. Med.*, 1997, **8**(11), 707–712.
26 B. D. Smith and D. A. Grande, The current state of scaffolds for musculoskeletal regenerative applications, *Nat. Rev. Rheumatol.*, 2015, **11**(4), 213–222.
27 Z. Z. Zhang, D. Jiang, J. X. Ding, S. J. Wang, L. Zhang, J. Y. Zhang, *et al.*, Role of scaffold mean pore size in meniscus regeneration, *Acta Biomater.*, 2016, **43**, 314–326.
28 P. Buma, M. van Meel, T. G. van Tienen and R. P. H. Veth, Tissue Engineering of the Meniscus, in *Musculoskeletal Tissue Regeneration*, ed. W. S. Pietrzak, Humana Press, Totowa, NJ, 2008, pp. 327–346. DOI: 10.1007/978-1-59745-239-7_16.
29 C. A. Murphy, A. K. Garg, J. Silva-Correia, R. L. Reis, J. M. Oliveira and M. N. Collins, The meniscus in normal and osteoarthritic tissues: facing the structure property challenges and current treatment trends, *Annu. Rev. Biomed. Eng.*, 2019, **21**(1), 495–521.
30 A. A. M. Dhollander, V. Condello, V. Madonna, M. Bonomo and P. Verdonk, Meniscal Augmentation and Replacement (Menaflex, Actifit, and NUsurface), in *Cartilage Restoration: Practical Clinical Applications*, ed. J. Farr and A. H. Gomoll, Springer International Publishing, Cham, 2018, pp. 371–382. DOI: 10.1007/978-3-319-77152-6_28.
31 J. Sun, S. Vijayavenkataraman and H. Liu, An overview of scaffold design and fabrication technology for engineered knee meniscus, *Materials*, 2017, **10**(1), 29.
32 L. Kluyskens, P. Debieux, K. L. Wong, A. J. Krych and D. B. F. Saris, Biomaterials for meniscus and cartilage in knee surgery: state of the art, *J. ISAKOS*, 2022, **7**(2), 67–77.
33 C. Ghisa and K. R. Zaslav, Current state of off the shelf scaffolds and implants for meniscal replacement, *J. Cartil. Jt. Preserv.*, 2022, **2**(1), 100040.
34 T. V. Tienen, K. C. Defoort, S. van de Groes, P. Emans, P. Heesterbeek and R. Pikaart, The first clinical experiences with an anatomically shaped artificial medial meniscus prosthesis for the knee, *Orthop. Proc.*, 2021, **103-B**(SUPP_9), 10–10.
35 A. Houben, P. Roose, H. Van den Bergen, H. Declercq, J. Van Hoorick, P. Gruber, *et al.*, Flexible oligomer spacers as the key to solid-state photopolymerization of hydrogel precursors, *Mater. Today Chem.*, 2017, **4**, 84–89.
36 A. Mignon, D. Pezzoli, E. Prouve, L. Levesque, A. Arslan, N. Pien, *et al.*, Combined effect of LAPONITE® and polymer molecular weight on the cell-interactive properties of synthetic PEO-based hydrogels, *React. Funct. Polym.*, 2019, **136**, 95–106.
37 A. Bacchi and C. S. Pfeifer, Rheological and mechanical properties and interfacial stress development of composite cements modified with thio-urethane oligomers, *Dent. Mater.*, 2016, **32**(8), 978–986.
38 H. Seyednejad, D. Gawlitta, W. J. A. Dhert, C. F. van Nostrum, T. Vermonden and W. E. Hennink, Preparation and characterization of a three-dimensional printed scaffold based on a functionalized polyester for bone tissue engineering applications, *Acta Biomater.*, 2011, **7**(5), 1999–2006.
39 L. Moroni, J. R. de Wijn and C. A. van Blitterswijk, 3D fiber-deposited scaffolds for tissue engineering: influence of pores geometry and architecture on dynamic mechanical properties, *Biomaterials*, 2006, **27**(7), 974–985.
40 R. Landers, A. Pfister, U. Hubner, H. John, R. Schmelzeisen and R. Mulhaupt, Fabrication of soft tissue engineering scaffolds by means of rapid prototyping techniques, *J. Mater. Sci.*, 2002, **37**(15), 3107–3116.
41 J. Van Hoorick, P. Gruber, M. Markovic, M. Tromayer, J. Van Erps, H. Thienpont, *et al.*, Cross-linkable gelatins with superior mechanical properties through carboxylic acid modification: increasing the two-photon polymerization potential, *Biomacromolecules*, 2017, **18**(10), 3260–3272.
42 T. Desmet, T. Billiet, E. Berneel, R. Cornelissen, D. Schaubroeck, E. Schacht, *et al.*, Post-plasma grafting of AEMA as a versatile tool to biofunctionalise polyesters for tissue engineering, *Macromol. Biosci.*, 2010, **10**(12), 1484–1494.

Open Access Article. Published on 21 January 2026. Downloaded on 5/27/2026 2:20:44 AM. This article is licensed under a Creative Commons Attribution-NonCommercial 3.0 Unported Licence.

43 International Organization for Standardization I, *ISO 10993-5: Biological evaluation of medical devices - Part 5: Test for in vitro cytotoxicity*, Geneva, Switzerland, 2009.
44 G. Bahcecioglu, N. Hasirci, B. Bilgen and V. Hasirci, A 3D printed PCL/hydrogel construct with zone-specific biochemical composition mimicking that of the meniscus, *Biofabrication*, 2019, **11**(2), 025002.
45 M. A. Woodruff and D. W. Hutmacher, The return of a forgotten polymer—polycaprolactone in the 21st century, *Prog. Polym. Sci.*, 2010, **35**(10), 1217–1256.
46 A. Dhollander, P. Verdonk and R. Verdonk, Treatment of painful, irreparable partial meniscal defects with a polyurethane scaffold: midterm clinical outcomes and survival analysis, *Am. J. Sports Med.*, 2016, **44**(10), 2615–2621.
47 J. J. Elsner, M. Shemesh, A. Shefy-Peleg, Y. Gabet, E. Zylberberg and E. Linder-Ganz, Quantification of in vitro wear of a synthetic meniscus implant using gravimetric and micro-CT measurements, *J. Mech. Behav. Biomed. Mater.*, 2015, **49**, 310–320.
48 R. Verdonk, P. Verdonk, W. Huysse, R. Forsyth and E. L. Heinrichs, Tissue ingrowth after implantation of a novel, biodegradable polyurethane scaffold for treatment of partial meniscal lesions, *Am. J. Sports Med.*, 2011, **39**(4), 774–782.
49 M. Pergal and M. Balaban, Synthesis and structure-property relationships of biodegradable polyurethanes, in *Biodegradable Polymers: recent developments and new perspectives*, IAPC Publishing, Zagreb, Croatia, 2017, pp. 141–190.
50 R. G. J. C. Heijkants, R. V. van Calck, T. G. van Tienen, J. H. de Groot, P. Buma, A. J. Pennings, *et al.*, Uncatalyzed synthesis, thermal and mechanical properties of polyurethanes based on poly(ε-caprolactone) and 1,4-butane diisocyanate with uniform hard segment, *Biomaterials*, 2005, **26**(20), 4219–4228.
51 I. M. El-Sherbiny and M. H. Yacoub, Hydrogel scaffolds for tissue engineering: progress and challenges, *Glob. Cardiol. Sci. Pract.*, 2013, **2013**(3), 316–342.
52 A. Houben, N. Pien, X. Lu, F. Bisi, J. Van Hoorick, M. N. Boone, *et al.*, Indirect solid freeform fabrication of an initiator-free photocrosslinkable hydrogel precursor for the creation of porous scaffolds, *Macromol. Biosci.*, 2016, **16**(12), 1883–1894.
53 A. Arslan, P. Roose, A. Houben, H. Declercq, S. Van Vlierberghe and P. Dubruel, Printability evaluation of UV-curable aqueous LAPONITE®/urethane-based PEG inks, *ACS Appl. Polym. Mater.*, 2023, **5**(4), 2345–2358.
54 H. R. Kricheldorf, Syntheses of biodegradable and biocompatible polymers by means of bismuth catalysts, *Chem. Rev.*, 2009, **109**(11), 5579–5594.
55 N. C. Padmavathi and P. R. Chatterji, Structural characteristics and swelling behavior of poly(ethylene glycol) diacrylate hydrogels, *Macromolecules*, 1996, **29**(6), 1976–1979.
56 K. Pielichowski and K. Flejtuch, Differential scanning calorimetry studies on poly(ethylene glycol) with different molecular weights for thermal energy storage materials, *Polym. Adv. Technol.*, 2002, **13**(10–12), 690–696.
57 X. Chen, G. Hou, Y. Chen, K. Yang, Y. Dong and H. Zhou, Effect of molecular weight on crystallization, melting behavior and morphology of poly(trimethylene terephalate), *Polym. Test.*, 2007, **26**(2), 144–153.
58 M. J. Jenkins and K. L. Harrison, The effect of molecular weight on the crystallization kinetics of polycaprolactone, *Polym. Adv. Technol.*, 2006, **17**(6), 474–478.
59 Y. Wang, C. Li, X. Tuo, Y. Gong and J. Guo, Polyethylene glycol modified epoxy acrylate UV curable 3D printing materials, *J. Appl. Polym. Sci.*, 2020, **138**(13), 1–8.
60 E. O. Bachtiar, O. Erol, M. Millrod, R. Tao, D. H. Gracias, L. H. Romer, *et al.*, 3D printing and characterization of a soft and biostable elastomer with high flexibility and strength for biomedical applications, *J. Mech. Behav. Biomed. Mater.*, 2020, **104**, 103649.
61 N. Celikkin, S. J. Padial, M. Costantini, H. Hendrikse, R. Cohn, C. J. Wilson, *et al.*, 3D printing of thermoresponsive polyisocyanide (PIC) hydrogels as bioink and fugitive material for tissue engineering, *Polymers*, 2018, **10**(5), 555.
62 S. Jain, T. Fuoco, M. A. Yassin, K. Mustafa and A. Finne-Wistrand, Printability and critical insight into polymer properties during direct-extrusion based 3D printing of medical grade polylactide and copolyesters, *Biomacromolecules*, 2020, **21**(2), 388–396.
63 L. K. Narayanan and R. A. Shirwaiker, Experimental characterization and finite element modeling of the effects of 3D bioplotting process parameters on structural and tensile properties of polycaprolactone (PCL) scaffolds, *Appl. Sci.*, 2020, **10**(15), 5289.
64 J. Aho, J. P. Boetker, S. Baldursdottir and J. Rantanen, Rheology as a tool for evaluation of melt processability of innovative dosage forms, *Int. J. Pharm.*, 2015, **494**(2), 623–642.
65 A. Das, E. L. Gilmer, S. Biria and M. J. Bortner, Importance of polymer rheology on material extrusion additive manufacturing: correlating process physics to print properties, *ACS Appl. Polym. Mater.*, 2021, **3**(3), 1218–1249.
66 K. Wang, Die Swell of Complex Polymeric Systems, in *Viscoelasticity*, ed. J. de Vicente, IntechOpen, Rijeka, 2012, ch. 4, DOI: 10.5772/50137.
67 J. Klompmaker, H. W. Jansen, R. P. Veth, H. K. Nielsen, J. H. de Groot and A. J. Pennings, Porous implants for knee joint meniscus reconstruction: a preliminary study on the role of pore sizes in ingrowth and differentiation of fibrocartilage, *Clin. Mater.*, 1993, **14**(1), 1–11.
68 T. G. Tienen, R. G. J. C. Heijkants, J. H. de Groot, A. J. Schouten, A. J. Pennings, R. P. H. Veth, *et al.*, Meniscal replacement in dogs. Tissue regeneration in two different materials with similar properties, *J. Biomed. Mater. Res., Part B*, 2006, **76B**(2), 389–396.
69 Q. Hamid, J. Snyder, C. Wang, M. Timmer, J. Hammer, S. Guceri, *et al.*, Fabrication of three-dimensional scaffolds using precision extrusion deposition with an assisted cooling device, *Biofabrication*, 2011, **3**(3), 034109.

 This journal is © The Royal Society of Chemistry 2026

Open Access Article. Published on 21 January 2026. Downloaded on 5/27/2026 2:20:44 AM. This article is licensed under a Creative Commons Attribution-NonCommercial 3.0 Unported Licence.

70 T. Serra, J. A. Planell and M. Navarro, High-resolution PLA-based composite scaffolds via 3-D printing technology, *Acta Biomater.*, 2013, **9**(3), 5521–5530.
71 L. Van Damme, E. Briant, P. Blondeel and S. Van Vlierberghe, Indirect versus direct 3D printing of hydrogel scaffolds for adipose tissue regeneration, *MRS Adv.*, 2020, **5**(17), 855–864.
72 S. Zhu, G. Tong, J. Xiang, S. Qiu, Z. Yao, X. Zhou, *et al.*, Microstructure analysis and reconstruction of a meniscus, *Orthop. Surg.*, 2021, **13**(1), 306–313.
73 H. Pereira, S. G. Caridade, A. M. Frias, J. Silva-Correia, D. R. Pereira, I. F. Cengiz, *et al.*, Biomechanical and cellular segmental characterization of human meniscus: building the basis for tissue engineering therapies, *Osteoarthritis Cartilage*, 2014, **22**(9), 1271–1281.
74 L. Moroni, F. M. Lambers, W. Wilson, C. C. van Donkelaar, J. R. de Wijn, R. Huiskesb, *et al.*, Finite element analysis of meniscal anatomical 3D scaffolds: implications for tissue engineering, *Open Biomed. Eng. J.*, 2007, **1**, 23–34.
75 L. Tytgat, L. Van Damme, J. Van Hoorick, H. Declercq, H. Thienpont, H. Ottevaere, *et al.*, Additive manufacturing of photo-crosslinked gelatin scaffolds for adipose tissue engineering, *Acta Biomater.*, 2019, **94**, 340–350.
76 Q. T. Nguyen, Y. Hwang, A. C. Chen, S. Varghese and R. L. Sah, Cartilage-like mechanical properties of poly (ethylene glycol)-diacrylate hydrogels, *Biomaterials*, 2012, **33**(28), 6682–6690.
77 S. Pahoff, C. Meinert, O. Bas, L. Nguyen, T. J. Klein and D. W. Hutmacher, Effect of gelatin source and photo-initiator type on chondrocyte redifferentiation in gelatin methacryloyl-based tissue-engineered cartilage constructs, *J. Mater. Chem. B*, 2019, **7**(10), 1761–1772.
78 I. Silvestro, R. Sergi, A. S. D'Abusco, A. Mariano, A. Martinelli, A. Piozzi, *et al.*, Chitosan scaffolds with enhanced mechanical strength and elastic response by combination of freeze gelation, photo-crosslinking and freeze-drying, *Carbohydr. Polym.*, 2021, **267**, 118156.
79 M. Domingos, F. Intranuovo, T. Russo, R. D. Santis, A. Gloria, L. Ambrosio, *et al.*, The first systematic analysis of 3D rapid prototyped poly(ε-caprolactone) scaffolds manufactured through BioCell printing: the effect of pore size and geometry on compressive mechanical behaviour and in vitro hMSC viability, *Biofabrication*, 2013, **5**(4), 045004.
80 H. Zhao, L. Li, S. Ding, C. Liu and J. Ai, Effect of porous structure and pore size on mechanical strength of 3D-printed comby scaffolds, *Mater. Lett.*, 2018, **223**, 21–24.
81 C. A. Murphy, J. B. Costa, J. Silva-Correia, J. M. Oliveira, R. L. Reis and M. N. Collins, Biopolymers and polymers in the search of alternative treatments for meniscal regeneration: state of the art and future trends, *Appl. Mater. Today*, 2018, **12**, 51–71.
82 L. E. Bertassoni, M. Cecconi, V. Manoharan, M. Nikkhah, J. Hjortnaes, A. L. Cristino, *et al.*, Hydrogel bioprinted microchannel networks for vascularization of tissue engineering constructs, *Lab Chip*, 2014, **14**(13), 2202–2211.
83 S. L. Vega, M. Y. Kwon and J. A. Burdick, Recent advances in hydrogels for cartilage tissue engineering, *Eur. Cells Mater.*, 2017, **33**, 59–75.
84 B. Bilgen, C. T. Jayasuriya and B. D. Owens, Current concepts in meniscus tissue engineering and repair, *Adv. Healthc. Mater.*, 2018, **7**(11), 1701407.
85 A. C. AufderHeide and K. A. Athanasiou, Mechanical stimulation toward tissue engineering of the knee meniscus, *Ann. Biomed. Eng.*, 2004, **32**(8), 1161–1174.
86 A. Szojka, K. Lalh, S. H. J. Andrews, N. M. Jomha, M. Osswald and A. B. Adesida, Biomimetic 3D printed scaffolds for meniscus tissue engineering, *Bioprinting*, 2017, **8**, 1–7.